DYNAMIC GAS INJECTION

R. Herrmann-Heber, S. Reinecke, M. Meier, U. Hampel

FINAL REPORT

Table of Contents

1   Executive Summary

The previous investigations showed that the pulsed aeration leads to higher oxygen mass transfer rates in specific cases. In narrow aeration columns positive effects could be shown for higher pulsation frequencies whereas in the DN900 column these effects were only present for higher flow rates in low frequencies. Investigations of bubble size distributions showed that the bubble size is not the only factor leading to increased oxygen mass transfer rates and that the positive effects depend on the geometry and the liquid flow behavior in the reactor. Further experiments therefore are focused on fundamental investigation the liquid flow behavior during pulsed aeration. A new experimental setup was constructed to study these hydrodynamic effects in 2D to enable a better understand of the underlying effects.

Highlights of the project:

Mass transfer during pulsed aeration
- Numerical simulations showed potential mass transfer enhancements of up to 24%
- Experimental investigations (pilot scale, DN400, 4 m aeration depth) proved mass transfer enhancements of up to 8.5% (2 Hz pulsations) confirmed in experiments in pilot scale
- DN900 column experiments showed up to 16% higher k_La in clean water (0.5 Hz) and 6.5% in wastewater (0.25 Hz)
- Optimal pulsation frequency shows a dependence of experimental geometry
- 20% improved mass transfer in wastewater pilot plant (uncontrolled aeration)
- Application of mass transfer model and population balance modelling to improve mass transfer prediction (master thesis in 2021)
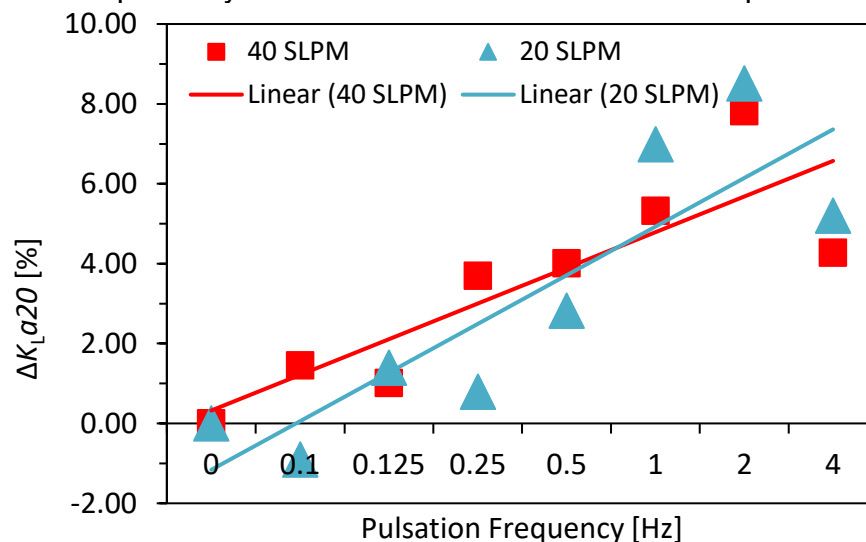- Model for scale-up and dynamic control needed and in development

Figure 1 K_La enhancement during pulsed aeration.

Hydrodynamics during pulsed aeration
- Higher pulsation frequencies can lead to smaller bubble sizes
- Favorable range of pulse frequency of 1 to 4 s^{-1} from lab experiments
- Ideal point of operation depends on system parameters (pulse frequency, gas flow rate, vessel/tank geometry, sparger configuration)

Hardware & software development
- Waterproof flow microscope prototype for measurements down to 4.5 m water depth
- First measurement of bubble size distributions in DN900 column under pulsations
- Improvement of flow microscope accuracy
- Flexible sparger concept from MILA project for spatial pulse patterns
- AI-assisted bubble recognition in images
- High potential synergies with project MILA and Advanced Process Control: align control of pulsed injection pattern with max. plant performance
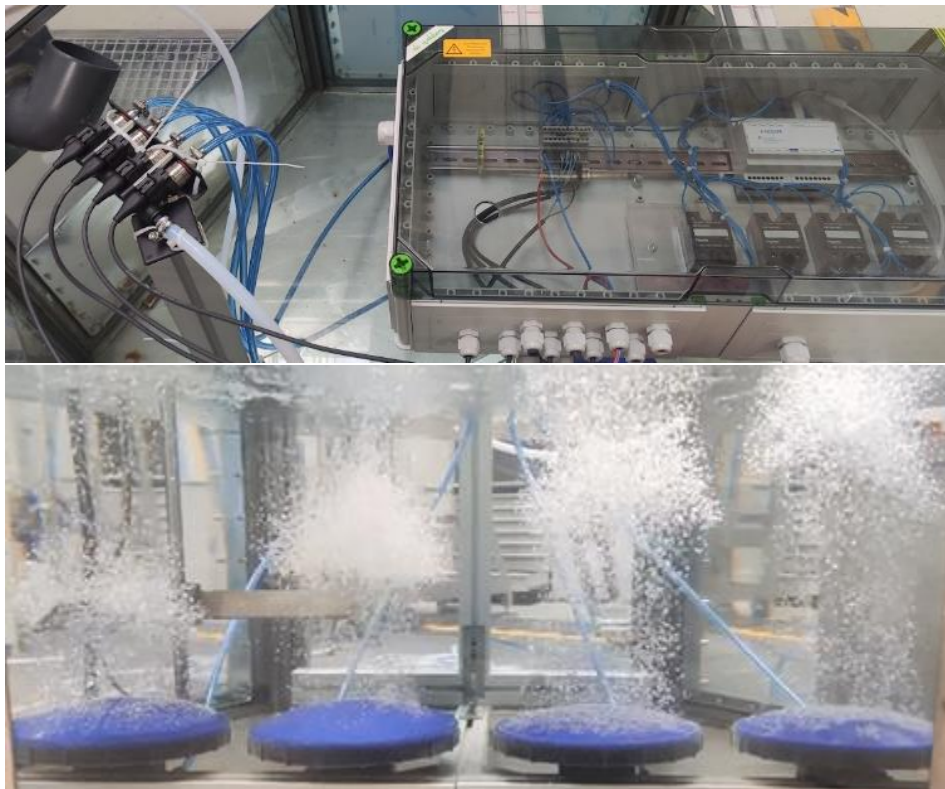

Figure 2 HZDR's flow microscope

Figure 3 New control setup for pulsed aeration.

2   Introduction & Project goal

The project is focused on development of innovative steps related to efficient gas transfer using low energy devices similar to fine bubble diffusers and spargers used in bioprocesses using yeast, bacteria, mammalian cells etc. to obtain value creation to industries such as treated wastewater, biopharma, fermentation and others. Dynamic (pulsed) gas injection regimes have been identified as promising candidate for improved mass transfer and mixing in (bio-) chemical processes. Sufficient understanding of the corresponding hydrodynamic and mass transfer mechanisms is required to explore the full potential of this unconventional injection regime. Therefore, the project includes a literature evaluation of fundamentals of gas injection in various bioprocesses, modelling and simulation, design and instrumentation of experimental setups and a strategic investigation.

3   Materials and Methods

The aim of the investigation is to identify the pulsation regimes that lead to the highest enhancements of the oxygen mass transfer and to find the changes in the hydrodynamic behavior that are responsible for the enhancements. Numerical simulations were conducted to explore aeration regimes with increases in mass transfer due to pulsation. This knowledge was then used to experimental investigations in different scales. Table 1 gives an overview on the parameters, which were investigated experimentally.

Table 1 Overview of experiments.

Setup	Investigated parameters	Media	Method/ technique
DN400	k_La, SOTR, SAE	Deionized water, air	Absorption method
	Gas hold-up (local, overall)		Wire-mesh sensor
	Bubble rise velocity		
DN900	k_La, SOTR, SAE	Deionized water, wastewater, air	Absorption method
	Bubble size and rise velocity		Flow microscope
2D column	k_La	Deionized water, air	Absorption method
	Bubble size and rise velocity		Videometry

3.1   Numerical Setup

A three-dimensional transient Euler-Euler simulation was used to simulate the mass transfer characteristics of gas-induced pulsed flow and compare it to continuous gas flow conditions. Bubble sizes between 2.0 and 4.0 mm, which are typical for membrane diffusers were considered in a mono-disperse model. Bubble break-up and coalescence was neglected, because of the unknown behavior in the pulsed bubble swarms. Three different gas flow rates were set in the simulation. For the test geometry, they are in a range, which is applicable for wastewater treatment. Low pulsation frequencies in the range of 0.1 to 4 Hz were used, due

to their possible application in wastewater treatment. The frequency range is chosen to include the frequencies that have been experimentally investigated in small scale setups before and is extended also to lower and higher frequencies.

For the determination of the mass transfer, the Two-Resistance model in ANSYS CFX was utilized. Both phases are considered as a mixture of two components and for the variable mass fraction of oxygen the scalar transport equation is solved:

$$\frac{\partial\left(\rho_k \alpha_k x_{O_2,k}\right)}{\partial t} + \nabla \cdot \left(\rho_k \alpha_k x_{O_2,k} \vec{u}_k\right) = \nabla \cdot \left(\alpha_k \left(\rho_k D_{O_2,k} + \frac{\mu_{T,k}}{Sc_{T,k}}\right) \nabla x_{O_2,k}\right) \pm \Gamma_{O_2,gl} \qquad 1$$

The turbulent Schmidt number $Sc_{T,K}$ is set to the standard value of 0.9 and the oxygen interphase mass transfer source term $\Gamma_{O_2,gl}$ was calculated by:

$$\frac{\left(\partial x_{O_2}\right)}{\partial t} = \Gamma_{O_2,gl} = k_L \, a_g \left[p_l x_{o,l}^* - \rho_l x_{o,l}\right] \qquad 2$$

The volumetric mass transfer coefficient and the specific interfacial area were determined according to

$$k_L = 2\sqrt{\frac{D_L}{\pi}} \left(\frac{\varepsilon}{\nu_L}\right)^{0.25} \qquad 3$$

and

$$a_g = 6\frac{\alpha_g}{d_B} \qquad 4$$

The model for the volumetric mass transfer coefficient is derived from Higbie's penetration theory and commonly used in numerical simulations and experimental investigations of bubbly flows. The interfacial area is calculated with equation 4 according to Deckwer.

Each of the both phases contain a constrained component to balance the mass fraction sum (equations 5 and 6). In the gaseous phase nitrogen and in the liquid phase water were considered as constraint components.

$$x_{O_2,g} + x_{N_2,g} = 1 \qquad 5$$

$$x_{O_2,l} + x_{w,l} = 1 \qquad\qquad\qquad 6$$

For the interphase forces and turbulence modelling the so-called baseline model with mono-disperse setup was used. A compilation of the employed models can be found in Table 2. These interphase forces define the coupling between the liquid and the gaseous phase. The drag force models the friction between the phases. It determines the rise velocity of the bubbles together with the lift force and play an important role in all relative movements of the two phases. The virtual mass force takes in account, that the rising bubble accelerates the surrounding liquid. The inertia of the liquid phase mass encountered by the accelerating bubbles exerts a virtual mass force on the bubbles. The lift force acts lateral to the flow direction and reflects the complex interaction between bubbles and the liquid velocity field. The turbulent dispersion force describes the effect of turbulent velocity fluctuations and their action on the spatial dispersion of the gaseous phase.

Table 2 Compilation of interphase forces and turbulence force used

Force/Model	Ref
Drag force	Ishii und Zuber (1979)
Lift force	Tomiyama (2002)
Virtual mass force	$C_{VM} = 0.5$
Turbulent dispersion force	Favre Averaged Drag Force
Turbulence of gas phase	Dispersed Phase Zero Equation model
Turbulence of liquid phase	SST model with automatic wall function
Bubble Induced Turbulence	Additional source terms in the k, ω equations of the SST model.
Turbulent viscosity	Rzehak (2013)

Numerical implementation and geometry

The CFD code presented before was numerically solved by ANSYS CFX 18.0. The high-resolution discretization of the partial and ordinary differential equations and a coupled volume fraction algorithm were used. They couple the equation for velocity, pressure and volume fraction. The two simulated test basins have a square base with a side length of 0.75 m and a height of 2 m and 4 m, respectively. A structured Cartesian grid with 72000 and respectively 144000 cells was applied to the test geometries, which results in a cell size of 25 x 25 x 25 mm. The test geometry is presented in Figure 4. The time step was set to 0.1 s with a total simulated time of 15000 s. The convergence criteria were specified with the root mean square level (RMS) of $1 \cdot 10^{-4}$ for all variables.

The gas inlet was modelled in the center of bottom of the test geometry with a size of 0.25 x 0.25 m. The oxygen mass fraction of the gas at the inlet was set to 23.1%. The bubble size at the inlet was set to 2.0, 3.2 and respectively 4.0 mm depending on the simulation case. The outlet was the entire area on top of the geometry with a degassing condition for the disperse phase and free slip condition for the continuous phase. The boundary condition of the test geometry walls was set to no slip. At the beginning of the transient simulation, the oxygen mass fraction in the liquid phase was 0%.

The gas mass flow rates for the pulsed aeration were implemented with rectangular waves for the whole frequency range of 0.1 to 4 Hz. This frequency range is close to the small-scale experimental investigations of Alkhalidi et al. (2016). The average gas mass flow rate of continuous and pulsed aeration was identical in all cases. This resulted in higher maximum mass flow rates in the pulsed aeration regimes, as shown in Figure 4. A compilation of the varied parameters in the simulations is listed in Table 3 Simulation parameters.
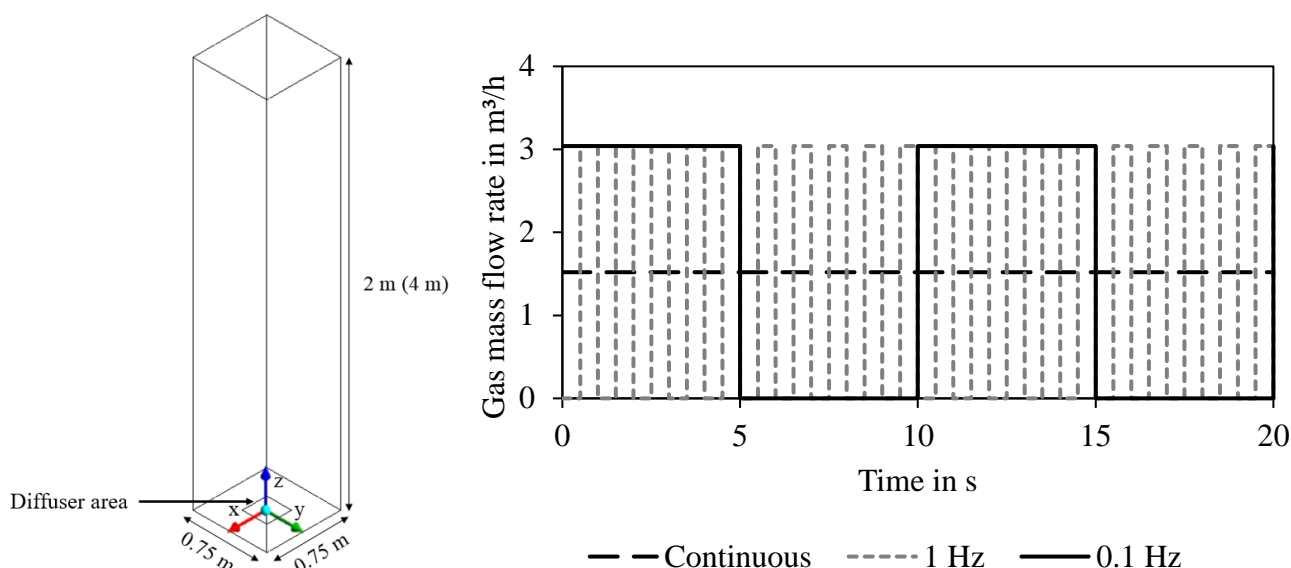

Figure 4 Test geometry with dimensions and origin of coordinates (left). Example of continuous and dynamic gas mass flow rates over time (right).

Table 3 Simulation parameters

Parameter	Used values
Gas flow rate	0.75; 1.50; 3.00 m³/h
Pulsation frequency	0 Hz (continuous aeration); 0.1; 0.125; 0.25; 0.5; 1; 2; 4 Hz
Aeration depth	2; 4 m
Bubble size	2.0; 3.2; 4.0 mm

3.2   Experimental Setups

3.2.1   Small Diameter Setup - DN400

The oxygen mass transfer behavior under aeration with pulsation was studied in the DN400 column with a water level of 4.1 m. It is filled with deionized water. An OTT D-Rex flexible membrane aerator is installed at the bottom of the column. Pressurized air was used with average flow rates ranging from 5.6 to 40 slpm. Pulsations were applied to the gas flow in the range of 0.1 Hz and 4 Hz and compared to continuous aeration.

The oxygen concentration was measured with two oxygen sensors in the column. For the calculation of oxygen mass transfer coefficients, the oxygen concentration curve was recorded according to the absorption method. This required the removal of oxygen by introducing nitrogen and afterwards the aeration with pressurized air. Furthermore, the inlet pressure was measured to enable the calculation of the standard aeration efficiency (SAE). The aim was to investigate the $k_L a$ enhancements, which were found in CFD simulations before.

Figure 5 DN400 bubble column setup.

3.2.2   Large Diameter Setup - DN900

The experimental investigation of the oxygen mass transfer during pulsed aeration is still on going. The experiments were transferred to the DN900 column to enable experiments under more realistic conditions including the use of wastewater. A smaller set of flow rates is being investigated with a focus on the experimental conditions, which were beneficial in the DN400 column. To confirm the results of the smaller column, the experiments are conducted in clean water and wastewater.

Figure 6 DN900 column.

9

3.2.3 2D Column

A narrow, rectangular bubble column was constructed to investigate the hydrodynamic behavior and mass transfer of bubbles rising during pulsed aeration in a quasi-2D case. This enables shadowgraphy experiments using high-speed cameras without many overlapping bubbles in the resulting images. Furthermore, the setup is equipped with a fast-response Unisense dissolved oxygen sensor. Polypropylene particles with a particle size of 100 μm are dissolved in the deionized water to enable the visualization of the liquid flows and the determination of turbulence.

3.3   Determination of Mass Transfer Rates

For the non-steady method of $K_L a$ determination, clean water or wastewater free of activated sludge may be used, so that no oxygen is consumed or produced via a biological reaction. Similar to the steady state method, the non-steady alternative also requires the reduction of the dissolved oxygen concentration to zero. Following this, air is then introduced into the vessel and the dissolved oxygen concentration of the water measured with diodes until saturation is achieved. An air-tight vessel is not required. Figure 7 presents a typical dissolved oxygen concentration curve for the non-steady state method.
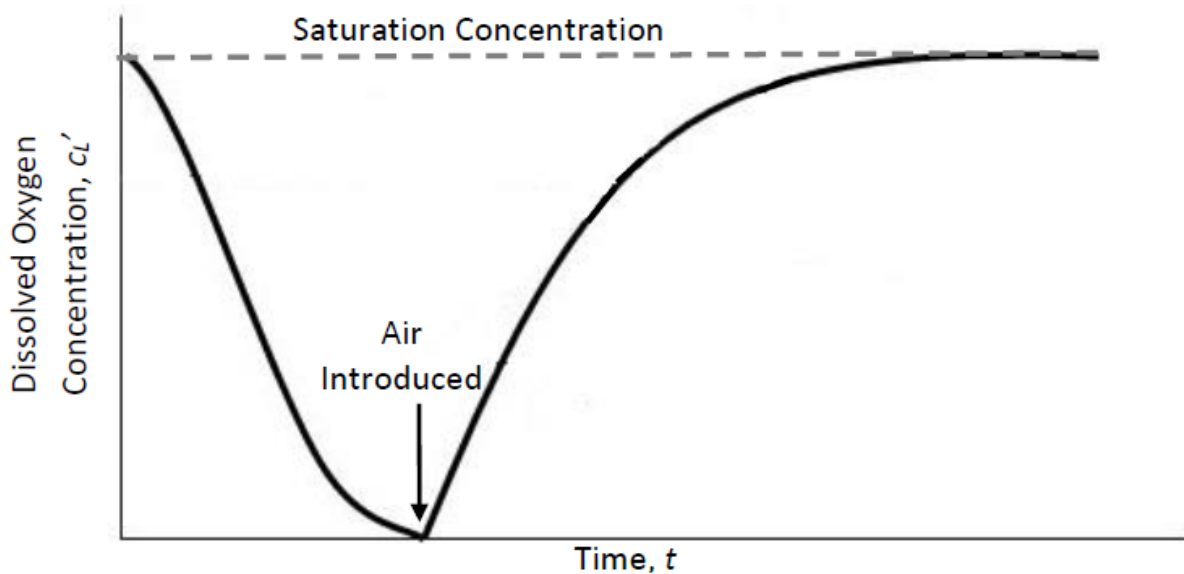
Figure 7 Concentration curve of an absorption test.

The dissolved oxygen concentration must be completely balanced by the mass transfer from the gas phase to the liquid, with the maximum achievable concentration being saturation, cs. If ideal mixing, negligible nitrogen counter diffusion, a constant interfacial area and no significant change in gas oxygen concentration are assumed then Equation 7 is valid:

$$\frac{dc'}{dt} = K_L a(c_s - c'_L)$$

7

Utilizing the initial conditions of $c_L'=0$ when $t=0$, Equation 7 can be solved to give the following:

$$\ln\left(\frac{c_s - c_L'}{c_s}\right) = -K_L a\, t$$

8

If the bulk liquid concentration is assumed to be equal everywhere (perfect mixing), $K_L a$ can be determined directly from Equation 8 by plotting $\ln\left[\frac{c_s - c_L'}{c_s}\right]$ against t. The straight-line gradient produced is equal to $K_L a$. Standards previously dictated that KLa measurements should be performed in this manner, using semi-log paper. However, the DWA standards have since been updated and it is now recommended that $K_L a$ values be determined using non-linear regression for parameters c_L' and t in Equation 7. It is therefore the non-steady method, with non-linear regression which has been implemented in this work.

3.4   Wire-Mesh Experiments

As described in Section 3.2.1, wire-mesh sensors (WMS) were implemented in the DN400 setup to determine the local gas holdup. Wire-mesh sensors are intrusive sensors which can measure fluid conductivity at several points. The sensors were designed, developed and built at HZDR. Both sensors consisted of two planes of 64 stainless-steel wires, with a 6.125 mm lateral spacing to form a mesh. The planes were aligned perpendicular to one another to create 4096 crossing points in total. One plane transmitted an electrical signal whilst the other plane acted as a receiver; the distance between the planes was 2 mm. One wire-mesh sensor was placed close to the aerator to capture the pulsation effect, whilst the other was placed near the top of the column to measure the change in bubble density over the column height.

For each crossing point, the mixture conductivity was measured over a period of 30 seconds with a measurement frequency of 2500 Hz. This measurement period was chosen to average out local fluctuations and to ensure that the full cycle of pulsations was captured. Measurements were taken across a range of air flowrates and pulsation frequencies. Each measurement generated a stack of conductivity data consisting of two spatial axes and one temporal axis, with a resolution of 64 by 64 pixels with 75,000 frames.

3.5   Determination of Bubble Properties

Bubble properties were determined by using optical methods. In the DN900 column the in-situ bubble tracking flow microscope was applied to record rising bubbles and determine their bubble size and rise velocity. In the 2D column setup a high-speed camera was placed at several locations to record bubbles. The bubble detection was conducted using self-implemented detection algorithms in case of the flow microscope. For the high-speed camera an

AI-assisted approach was used to due to the higher amount of overlapping bubbles in the images.

Bubble rise velocities were calculated by the displacement in x and y direction of bubbles in consecutive images. The same approach was used for the calculation of liquid velocities by tracking of particles in the images.

4 Results

4.1 Numerical Simulations

4.1.1 Effect of pulsation frequency

Figure 4 shows the local dissolved oxygen concentration curve after the start of the simulation at the center of the column for a pulsed aeration with 0.125 Hz and in comparison to continuous aeration for the same average gas mass flow rate. In the dynamic aeration regimes, the dissolved oxygen concentration profile shows high peaks in the moment when the gas flow reaches the column's center. This is visible in the gas hold-up at the monitor point, which is depicted in Figure 8 as well. In the case of dynamic aeration, the dissolved oxygen concentration follows the gas hold-up curve.
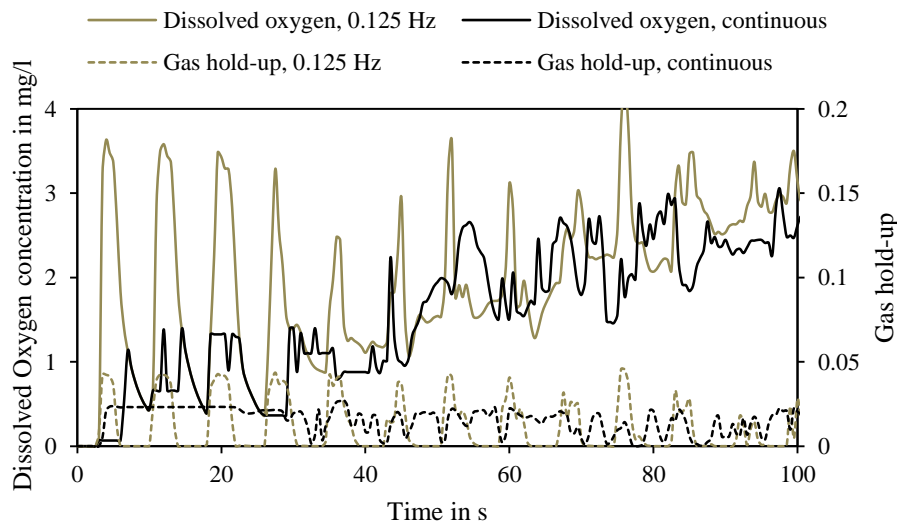
Figure 8 Dissolved oxygen concentration and local gas hold-up for continuous and dynamic aeration measured at a monitor point in the center of the test geometry.

There is a slight delay in the occurrence of the concentration and volume fraction peaks due to mass transfer and mixing in the liquid. For continuous aeration, the gas hold-up at the monitor point is fluctuating less. Fluctuations only occur due to bubble plume oscillations. Since the liquid oxygen mass fraction is 0 in the beginning of the simulation, the gas pulses with their high gas hold-up result in high dissolved oxygen concentration peaks due the stagnant liquid phase and high concentration gradients. As visible in Figure 9, the liquid velocity increases after the first pulses and the distribution of dissolved oxygen is improved. With

12

continuous aeration, the dissolved oxygen concentration in the center region is always higher in comparison to the surrounding liquid volume. In pulsed aeration, the gas flow is discontinuous and the center region has a lower dissolved oxygen concentration compared to the region closer to the wall. This is visible in Figure 9 at 10s. A new pulse of gas rises into an area with lower dissolved oxygen concentration. The higher local oxygen concentrations lead to high oxygen mass transfer. The local peaks in oxygen concentration in pulsed aeration with 0.125 Hz in Figure 8 indicate this as well.
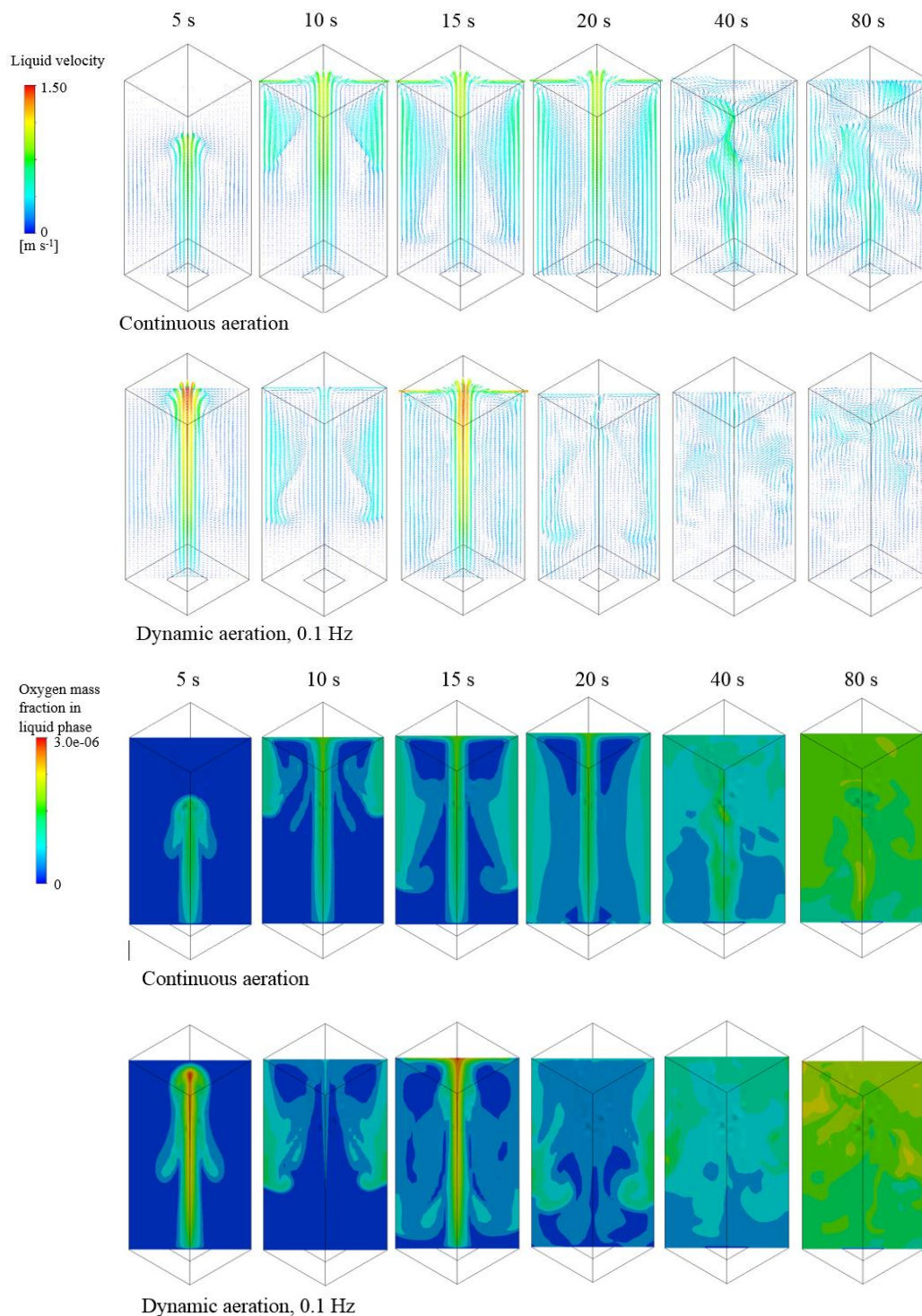
Figure 9 Liquid velocity fields (top) and dissolved oxygen mass fraction (bottom) for continuous aeration and pulsation with 0.1 Hz frequency and mean gas flow rate of 1.5 m³/h.

For the case with a gas mass flow rate of 1.5 m³/h, Figure 10 presents the volumetric mass transfer rates for continuous and dynamic aeration that have been determined by Equation 8 from the oxygen concentration curves. Furthermore, the increase of the $k_L a$ in comparison to the continuous case in percent is depicted as curve. The pulsations with 2 and 4 Hz show the highest $k_L a$ values among the tested pulsations. An increase of about 24% in volumetric mass transfer coefficient was determined for the pulsation with 2 Hz.
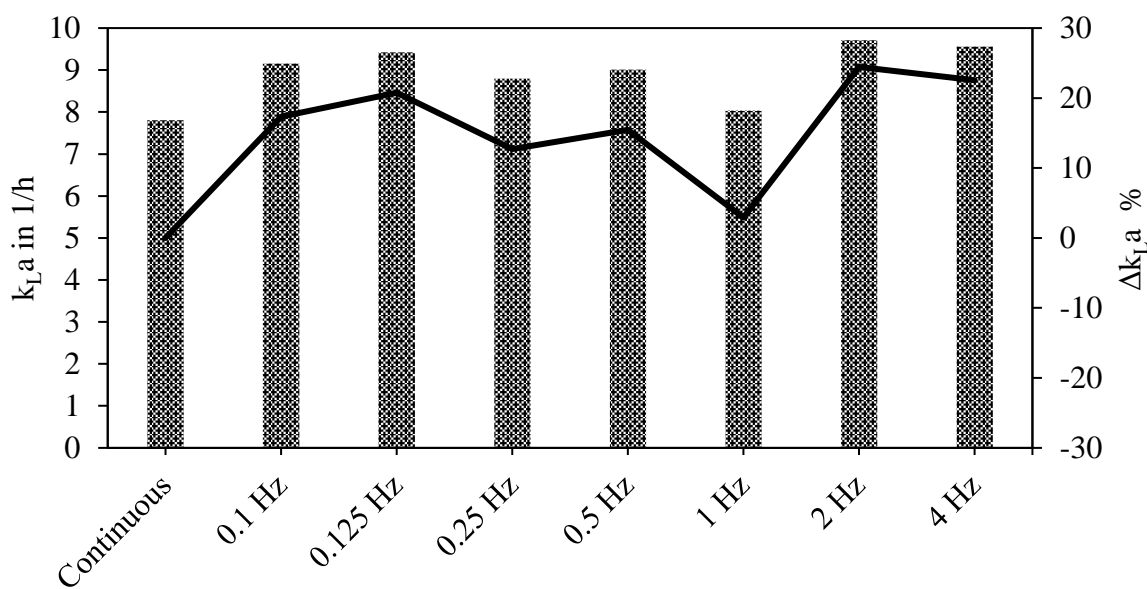
Figure 10 Comparison of volumetric mass transfer coefficients (bar chart) and its relative changes (line plot) for continuous aeration and dynamic aeration in the range of 0.1 to 4 Hz with an average gas mass flow rate of 1.5 m³/h.

Gas hold-up and the turbulent eddy dissipations are the influencing parameters of the mass transfer coefficient, despite the fixed parameters in these equations. A comparison of time averaged horizontal turbulent eddy dissipation profiles for different simulations is shown in Figure 11 Effect of pulsation frequency on time averaged turbulent eddy dissipation (x = 0, z = 1.5 m).. Only the pulsation with 4 Hz frequency surpasses the continuous aeration in the maximum turbulent eddy dissipation in the center of the test geometry. Low pulsation frequencies result in an eddy dissipation profile, which is more uniformly distributed. The gas phase distribution in this area is improved for the low pulsation frequencies as well, as shown in Figure 12. However, the effect of the turbulent eddy dissipation on the volumetric mass transfer coefficient is smaller than the effect of the gas hold-up.
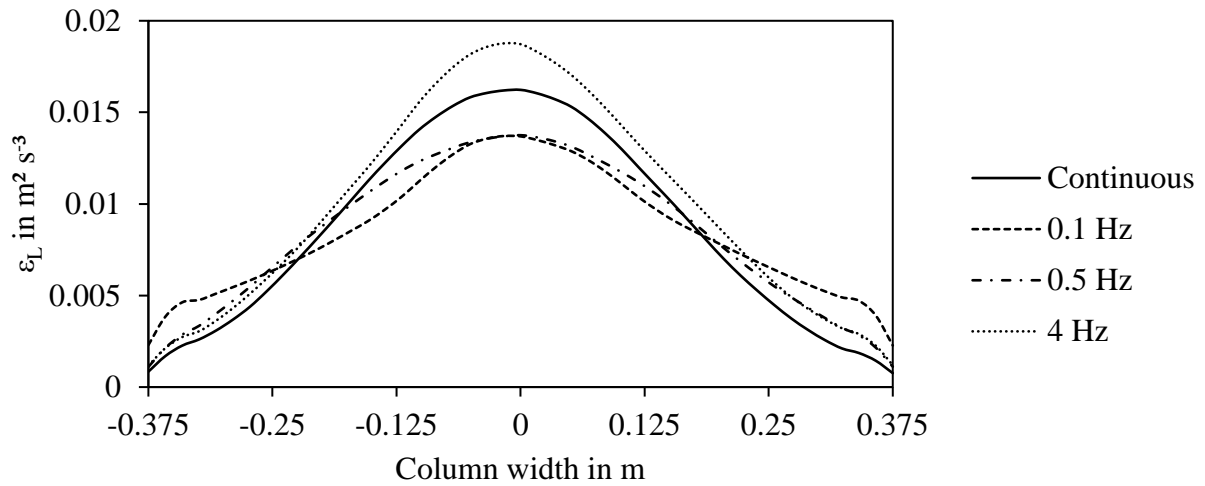
Figure 11 Effect of pulsation frequency on time averaged turbulent eddy dissipation (x = 0, z = 1.5 m).
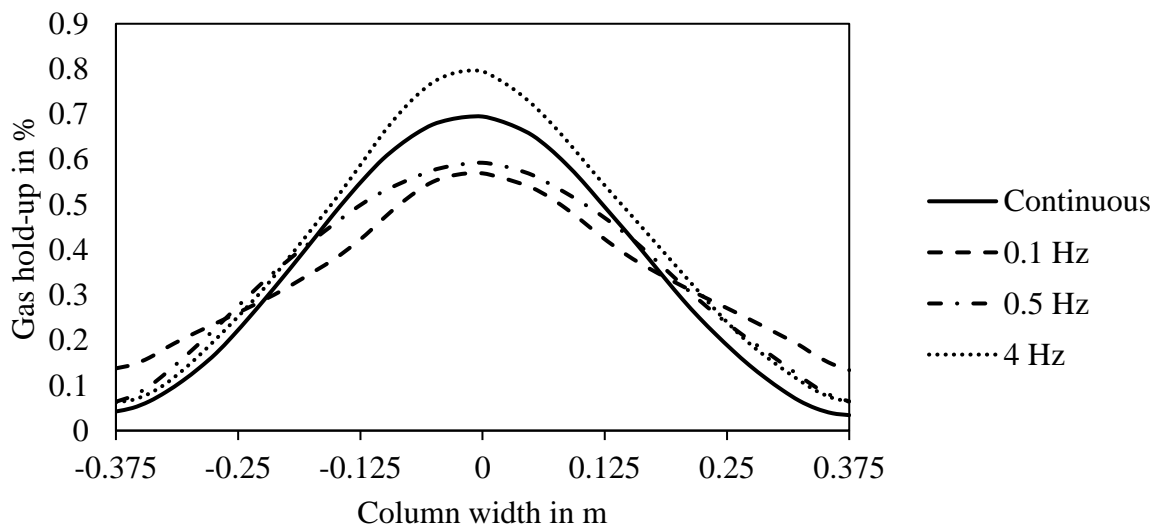
Figure 12 Effect of pulsation frequency on time averaged gas hold-up at 1.5 m liquid height.

Figure 13 shows the mean turbulent eddy dissipation and the gas hold-up for all simulations with 1.5 m³/h average flow rate. The gas hold-up curve correlates with the mass transfer curve in Figure 10. The drop in gas hold-up for 1 Hz pulsations indicates unfavorable macroscopic effects, which occur in this case. These macroscopic effects include higher liquid velocities in the center region, where the main part of the air bubbles rises as depicted in Figure 12. The higher velocities lead to lower residence times and therefore to lower gas hold-up. Only the faster pulsations have a positive effect on the mean turbulent eddy dissipation in comparison with the continuous aeration.
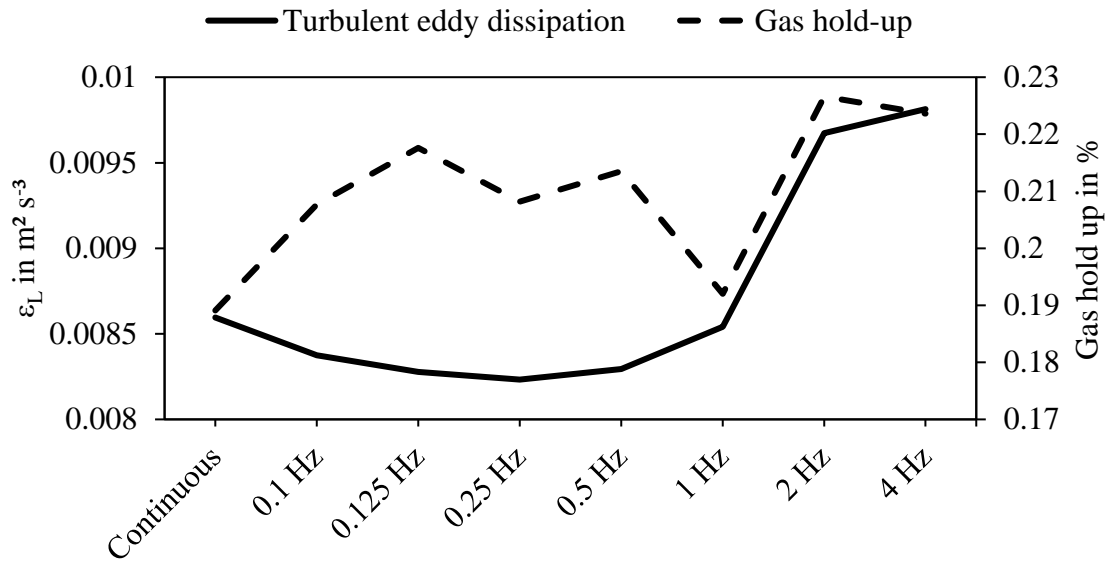
Figure 13 Mean turbulent eddy dissipation at a liquid height of 1.5 m and average gas hold up for simulations with mean flow rates of 1.5 m³/h.
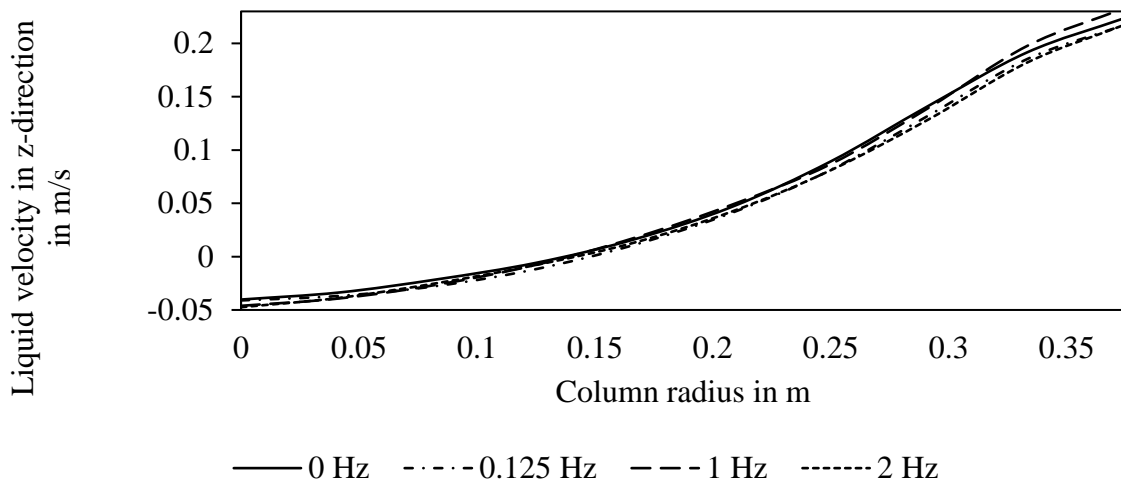
Figure 14 Radial profile of the time-averaged liquid velocity at 0.5 m height in 2 m geometry with 3.2 mm bubbles.

4.1.2   Flow rate

As typical for bubbly flows, the mass transfer depends on the gas mass flow rate. Figure 15 shows the dependency of the volumetric mass transfer coefficient on the gas mass flow rate. In every case, the mass transfer rates are higher for increased flow rates.
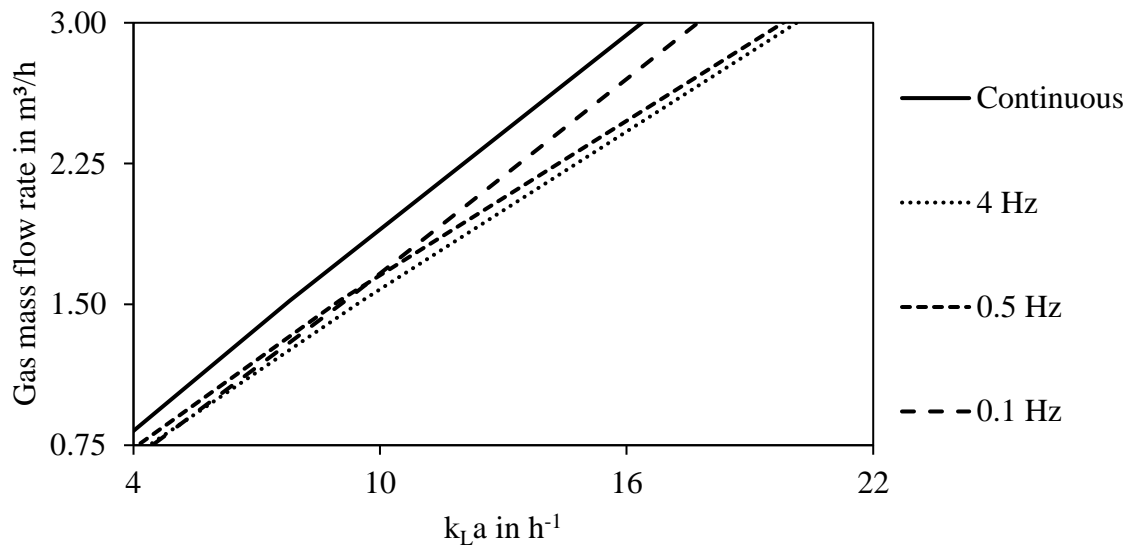
Figure 15 Inverted dependency of mass transfer rate on gas mass flow rate with 2 m liquid level (with bubble size of 3.2 mm).

Since the simulations use a mono-disperse setup, the higher gas flow rate directly correlates with higher interfacial area due to higher gas hold-up. Figure 16 shows the gas hold-up for a pulsed aeration with the three flow rates.
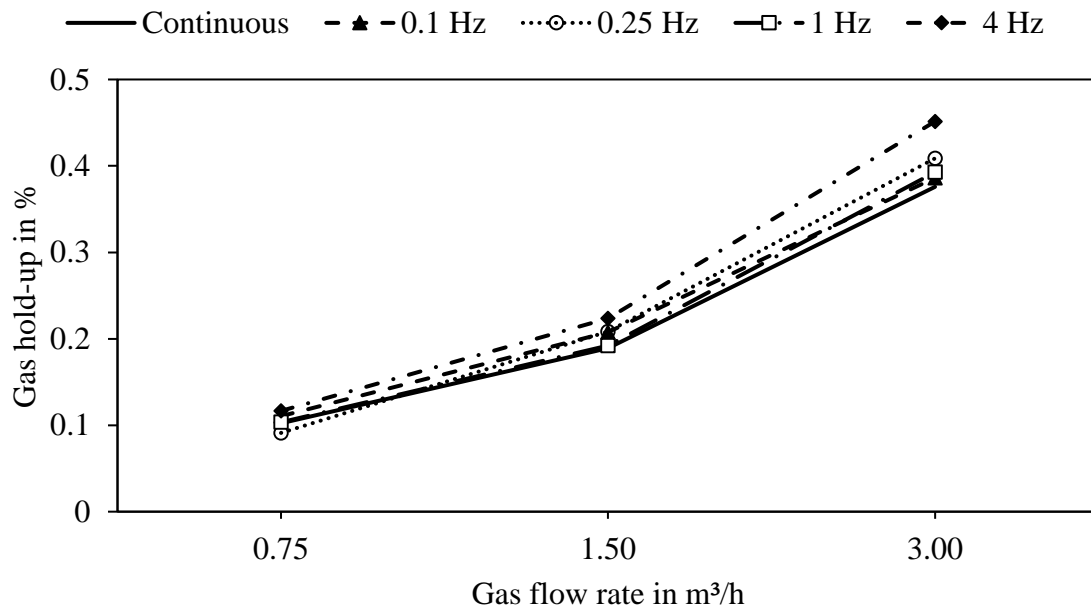
Figure 16 Comparison of gas hold-up with 0.75, 1.5 and 3.0 m³/h gas flow rate.

The k_La for the continuously aerated case is the lowest for the cases 1.5 and 3.0 m³/h gas flow rate. The low k_La at 0.75 m³/h and 0.25 Hz pulsed aeration shows that the pulsations

can decrease the gas hold-up as well. Whereas with the other pulsation regimes higher mass transfer coefficients are achieved. According to the graphs in Figure 15, it is possible to reach the equivalent mass transfer coefficients to continuous aeration with lower gas mass flow rates in the pulsed aeration. Whilst the continuously aerated test geometry achieves a k_La of 7.8 h^{-1} at 1.5 m³/h, the same mass transfer coefficient is possible with only 1.25 m³/h with a pulsation frequency of 4 Hz. The gas flow rate can be reduced by almost 16% while transferring the same amount of oxygen into the aeration basin.

4.2   DN400

4.2.1   Mass transfer

In Figure 17 the average mass transfer coefficients *kLa* determined in this investigation are depicted. It is visible that the kLa can be increased in aeration with pulsation in comparison with the steady/continuous aeration. For better viewability the diagrams in Figure 18 and Figure 19 are separated in high flow rate results (>20 slpm) and low flow rate results (<20 slpm).
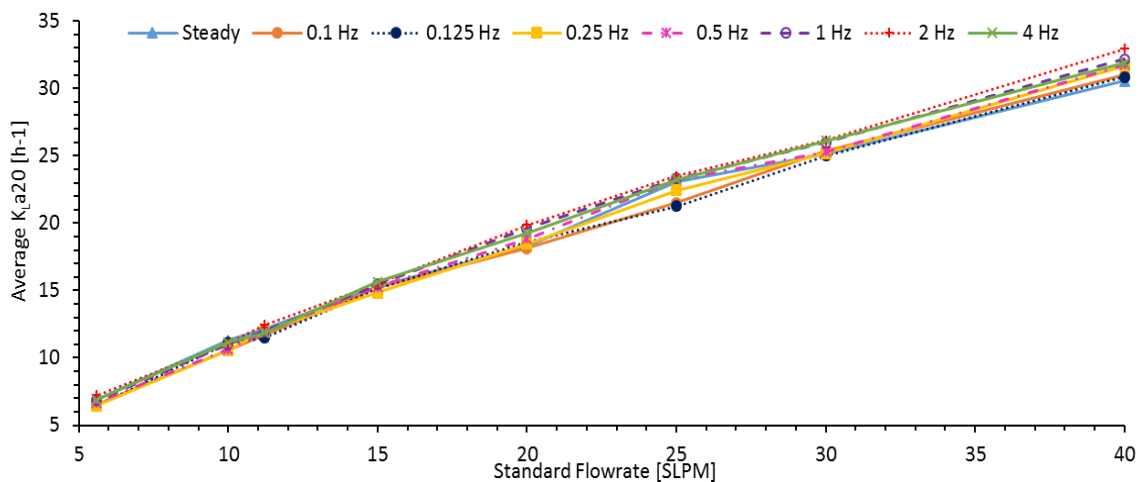
Figure 17 Comparison of average mass transfer coefficients kLa over the full range of flow rates.

Figure 18 shows the enhancement in mass transfer coefficients of the higher flow rates, which showed the largest improvements. The highest mass transfer rates could be achieved with pulsation frequencies of 2 Hz. An enhancement of the mass transfer coefficient by up to 8.5% was determined. The results show that higher frequencies generally show better results in all tested cases. This confirms the findings of the numerical simulations, which were presented in the former intermediate reports.
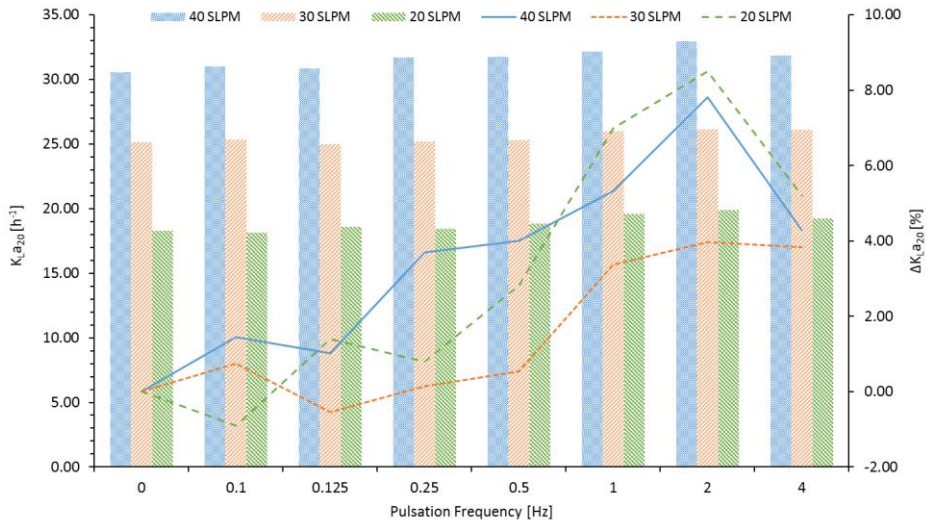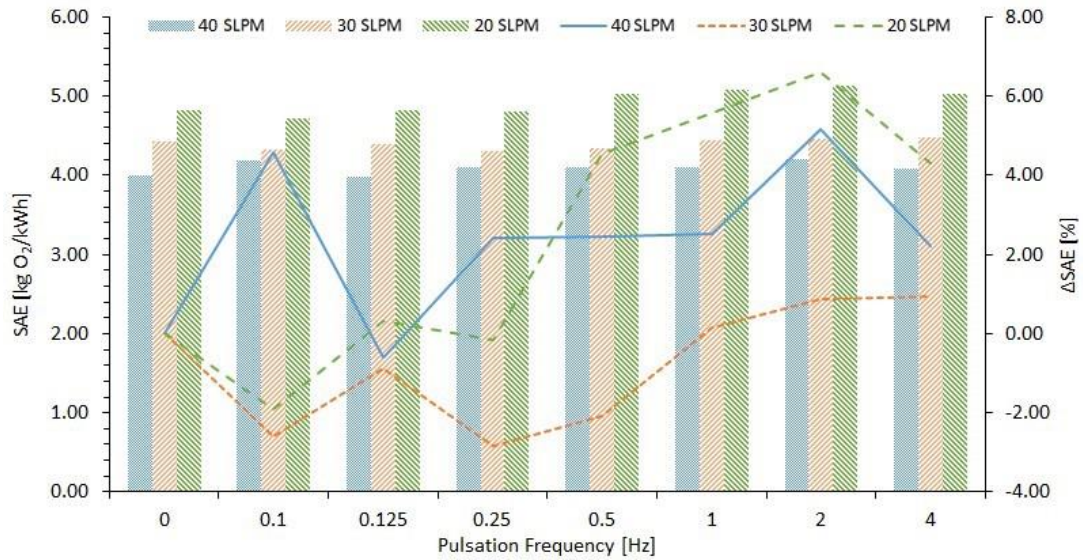
Figure 18 Comparison of the *kLa* values (bars, left axis) and enhancements (lines, right axis) of the higher flow rates. A pulsation frequency of 0 Hz represents the continuous aeration.

Figure 19 depicts the mass transfer coefficient and the enhancements for the lower flow rates in the range of 5.6 – 15 slpm. The pulsation frequency of 2 Hz also shows the best results in terms of oxygen mass transfer. However, the mass transfer coefficients for certain flow rates and pulsation frequencies are lower than the coefficients for the continuous aeration. This behaviour is still under investigation.
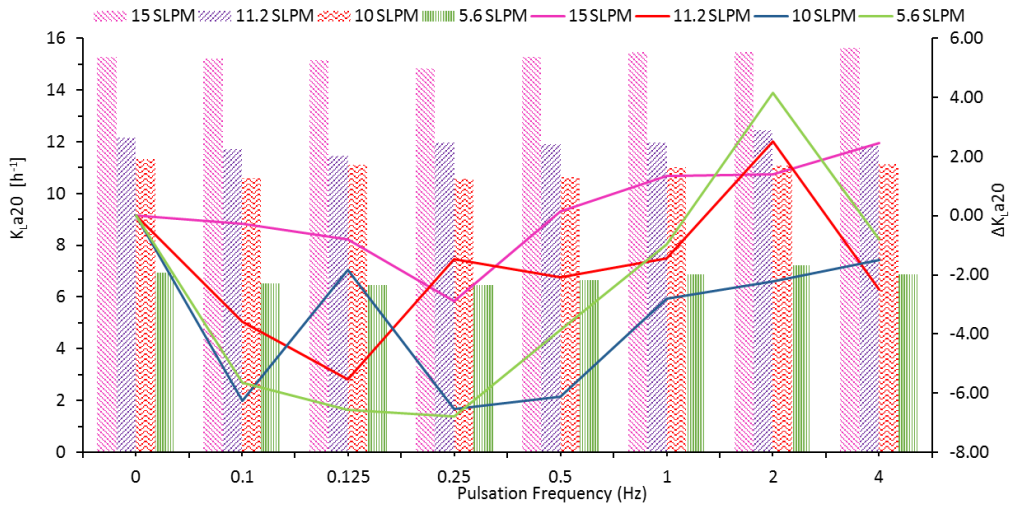
Figure 19 Comparison of the *kLa* values (bars, left axis) and enhancements (lines, right axis) of the lower flow rates. A pulsation frequency of 0 Hz represents the continuous aeration.

The standard aeration efficiency for the higher flow rates is depicted in Figure 20. The required electric energy for the aeration at these flow rates was calculated according to Pöpel and Wagner, 1994. The SAE enhancement curve clearly shows that the oxygen can be transferred to the liquid phase more efficiently by applying pulsations to the gas feed. Although the gas flow rate during the pulses is doubled compared to the continuous aeration, the pressure drop at the gas diffuser is only slightly increased (see Figure 22).

Figure 20 Comparison of the SAE values (bars, left axis) and their enhancements (lines, right axis) of the higher flow rates. A pulsation frequency of 0 Hz represents the continuous aeration.

4.2.2   Wire-mesh sensor

As presented in the previous section, the oxygen transfer is improved with pulsed aeration. However, the changes in the hydrodynamics that lead to this improvement are still unknown. Therefore, wire-mesh sensors were installed in the DN400 column to determine local hydrodynamic parameters such as the gas hold-up and the gas phase velocity. The investigation started in early November with two wire-mesh-sensors installed in the column to investigate the radial and axial distribution of the bubble swarm in the DN400 column.
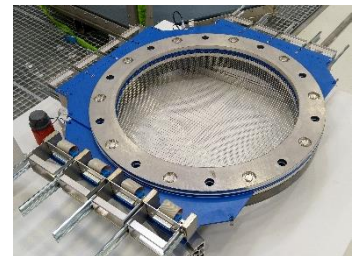
Figure 21 Picture of wire-mesh sensor.
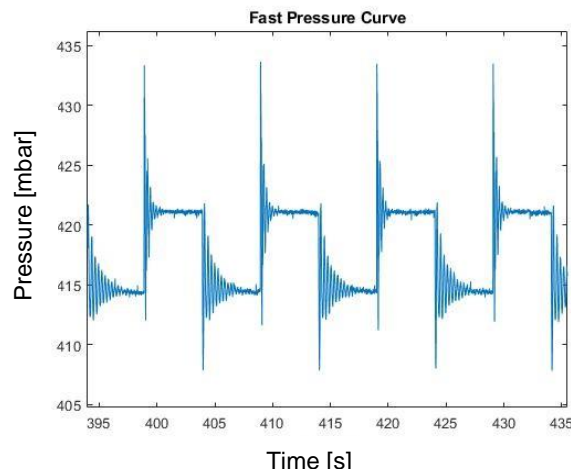
Figure 22 Example for pressure measured in the gas feed line before the gas diffuser (40 slpm, 0.1 Hz).

It was excepted that the mass transfer coefficients of pulsed aeration are higher due to higher gas hold-ups. Figure 23 shows an excerpt of the average gas hold-up determined for the DN400 column with the wire-mesh sensors. In contrast to the expectations the gas hold-up shows a greater enhancement for the low frequencies that did not achieve high enhancements in terms of oxygen mass transfer.
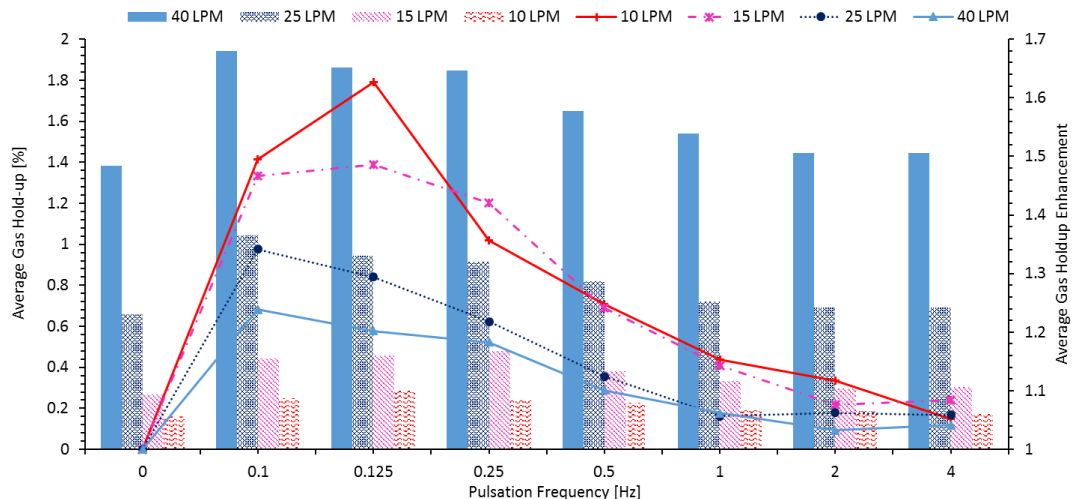
Figure 23 Average gas hold-up values (bars, left axis) and average gas hold-up enhancement (lines, right axis) in DN400 column obtained from wire-mesh measurements.

Therefore, an explanation of the improved oxygen mass transfer only with the averaged gas hold-up values is not possible. The investigation is focused on the changes in the local gas hold-up behavior and the gas distribution in the column. Furthermore, the bubble velocity at the two wire-mesh-planes is obtained from the measurements. These parameters will give further insights in the hydrodynamic changes due to pulsations and will allow model-based analysis of the influence of gas hold-up and bubble rise velocity on the oxygen mass transfer.

Figure 24 shows an example for the local cross-sectional distribution of the gas hold-up on the two wire-mesh-sensors in the DN400 column. It is visible that the radial distribution is wider and the axial distribution is dilated during the ascent of the bubble swarm in the column. These first results confirm the visual observations. The wire-mesh measurements are part of a master's thesis. The first set of experiments for the determination of the local gas hold-up has been finished and the bubble velocity measurement has started. The post-processing of the obtained data is ongoing.
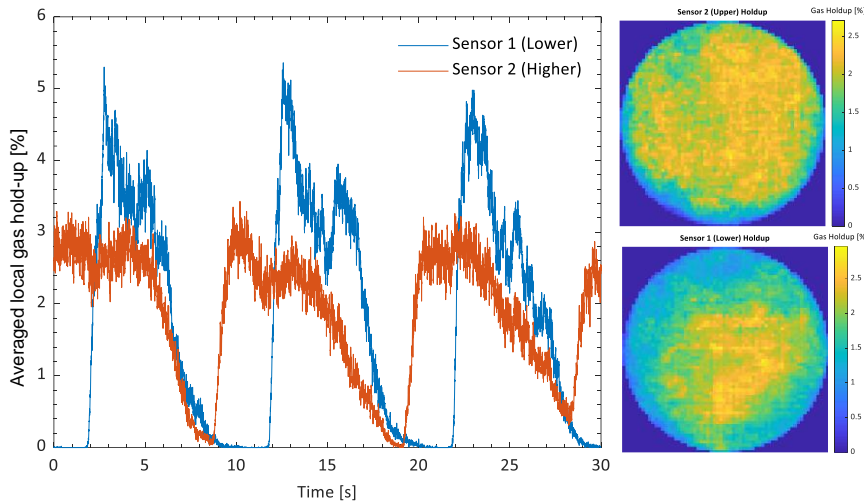
Figure 24 Example results of the wire-mesh-sensor measurements with pulsations.

4.3 DN900

4.3.1 Mass transfer

As part of an internship project, the implementation was validated and compared to actual mass transfer rates according to the manufacturer's datasheet. Therefore, the bubble sizes generated by Supratec Oxyflex MT300 diffusers were determined with the HZDR's flow microscope. These values were used as input parameters for the mass transfer model implementation to calculate the SSOTR. The comparison of the calculated values and the reported values for the diffuser are shown in Figure 25. In the range of the lower flow rates and lower bubble sizes, there is a good agreement with the reported SSOTR values. The deviation with the highest flow rate is probably a result of an underestimation of the bubble size due to the denser bubble swarm entering the microscope.
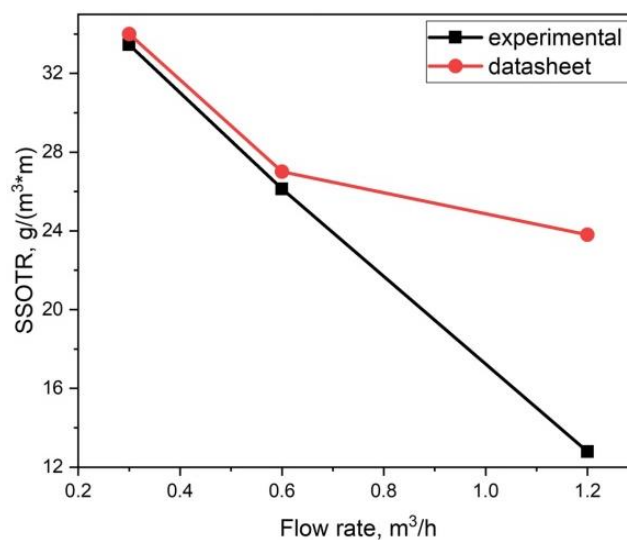
Figure 25 Comparison of plate diffuser SSOTR based on experimental results and SSOTR according to manufacturer's datasheet.

22

Furthermore, the results were compared to the optimal bubble size according to the literature, which was considered as physical limit for the oxygen mass transfer. Under the assumption that bubbles with optimal size can be generated at any flow rate the SAE was calculated and the results are depicted in Figure 26. It shows that the theoretical potential for improvements in aeration efficiency is still quite huge.
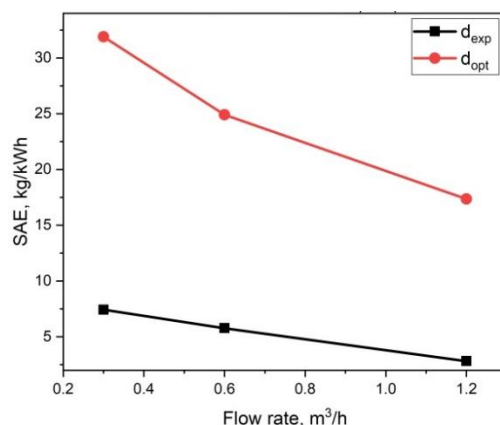
Figure 26 SAE of disc aerator calculated with experimental results of d_B (black line) and calculated based on assumption $d_B = 1\ mm$ (red line) at 5 cm height above aerator.

4.3.2 Bubble size

The HZDR flow microscope was first used in the DN900 columns to study bubble size distributions on various heights in the reactor. The investigations were aimed to find the changes in bubble size distributions due to pulsed aeration which lead to higher oxygen mass transfer coefficients. The bubble sizes were measured for pulsation frequencies between 0.1 to 4 Hz with 10-40 slpm air flow rate. Higher air flow rates were not suitable in this case due to too dense bubble flows, which could be processed in the image analysis. It was assumed that the pulsed aerations would lead to smaller bubble sizes and therefore increase the mass transfer rates. The results showed that the average bubble size does not shrink in the most cases. However, many pulsation frequencies showed bubble sizes that were just slightly larger although the air flow rate is twice as high during pulsation in comparison to continuous aeration (0 Hz in the diagram.)
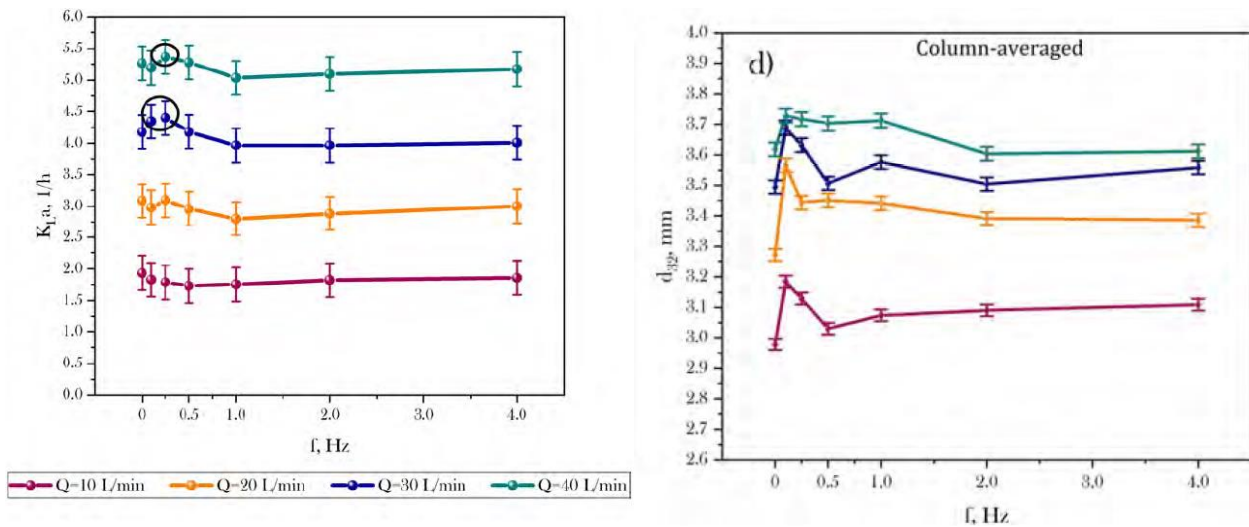
Figure 27 Mass transfer measurements using oxygen sensors showed mass transfer improvements for low frequencies in the case of DN900 reactor with low air flow rates and standard membrane diffusers.

5 Modelling

5.1 Population Balance Modelling

5.1.1 Fundamentals

The population balance framework is concerned with a system modeling consisting of a population of individual entities (e.g. flocs, bubbles, bacterial cells) interacting with their environmental phase in which they are dispersed (e.g. oxygen transfer from air bubble to the liquid phase, shear-induced breakup, or with one another e.g. breakup and coalescence). Such behavior may vary from particle to particle depending upon a number of specific properties (e.g. size, area, activity) that may be associated with the particle, change with time, and have an effect on the entity's interaction. To deal with properties indefinite or discreteness, the direct interactions between particles could be excluded while assuming the rate of change of state of any particle as a result of indirect interaction between particles via the continuous phase. As such, the behavior of the entity, and thus the behavior of the whole system is dependent on the "local" continuous phase properties and the ensemble of properties of each entity. According to Ramkrishna et.al, the system of particle states is generally characterized by a finite-dimensional vector and can only be changed due to evolutionary process (e.g. birth, death, dispersion) or due to transport of the entity phase in the system. This vector accounts for both external and internal coordinates, which may be used to describe the physical location of the center of mass of the particle and represents different quantities associated with the particle. Thus, the population balance model approach provides a statistical formulation able to describe the dispersed gaseous phase in a two-phase flow of aeration column. Analogously to the statistical Boltzmann transport equation the population balance equation (PBE) describes bubbles entering and leaving a control volume through different

24

mechanisms. These mechanisms can be: convection, evaporation or condensation (S_{sp}), breakup (S_b) or coalescence (S_c). In the most general form PBE can be expressed by the following equation:

$$\frac{\partial n}{\partial t} + \nabla_x \cdot \bar{u}n = S_{sp}(x, t) + S_b + S_c(x, t)$$

Where n is the number density function of the entity state vector at time t within the internal coordinates $\nabla_x \cdot \tilde{u}n$ is the growth rate of the particle and *h(x; t)* is termed to the net rate of generation of entities and represents all discrete processes. The first term on the left-hand side describes the rate of change in the number of bubbles also referred to as the accumulation term. The second term represents the rate of change of the number density due to entities transport governed by continuous processes (e.g. biomass growth, crystal growth) in the internal coordinates. The term on the right side of equation is the net rate of generation governed by discrete processes (e.g. breakup, coalescence, granulation).
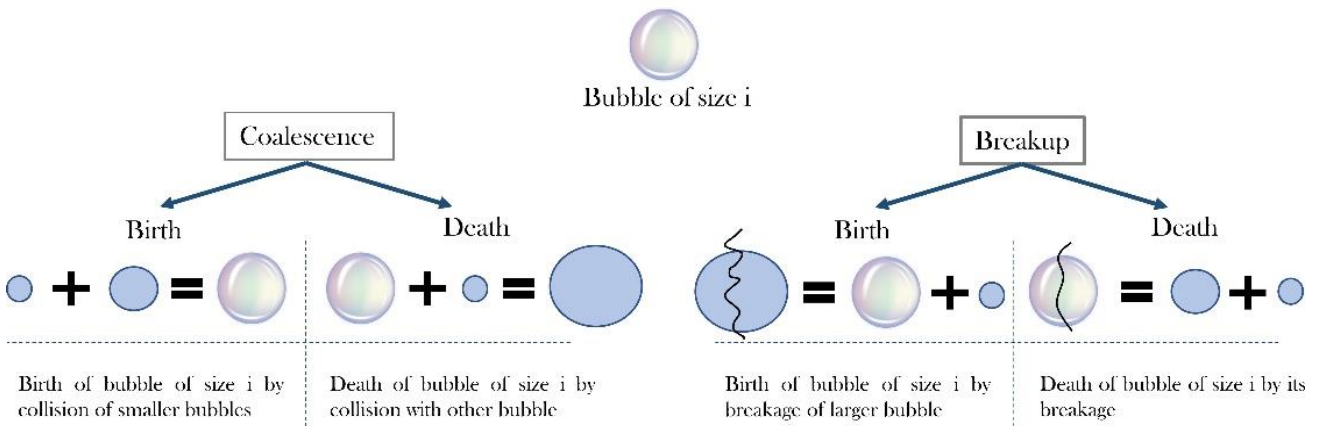
Figure 28 Schematic representation of mechanisms involved in breakup and coalescence (adapted from Nopens et.al)

If there is no evaporation or dissolution and a steady state is considered, the source term S_{sp} can be neglected. In the case of the bubble column, the evolution of particle number density distribution is driven by the destruction and creation of bubbles due to coalescence and breakage. These processes can be described by mathematical functions which are called kernels. Hence, the net rate of generation of entities is defined as:

$$S_c + S_b = S_c^+ + S_b^+ - S_b^-$$

Where the birth and the death rate of particles are denoted by '-' and '+' occurring due to coalescence and breakup processes - 'c' and 'b' respectively. The schematic representation of these different mechanisms through which particles can be formed and removed is visualized in the Figure 28.

5.1.2 Improved oxygen mass transfer modelling using population balance modelling

Due to break-up and coalescence the bubble size the bubble size varies during bubble rise the reactor/treatment plant. This effects the oxygen mass transfer. Standard mass transfer models assume one average bubble size for the prediction or calculation of the oxygen mass transfer coefficients. For more accurate results and better insight into changes due to pulsed aeration population balance models (PBM) were applied to predict changes in bubble sizes distributions over the height above the gas diffuser.
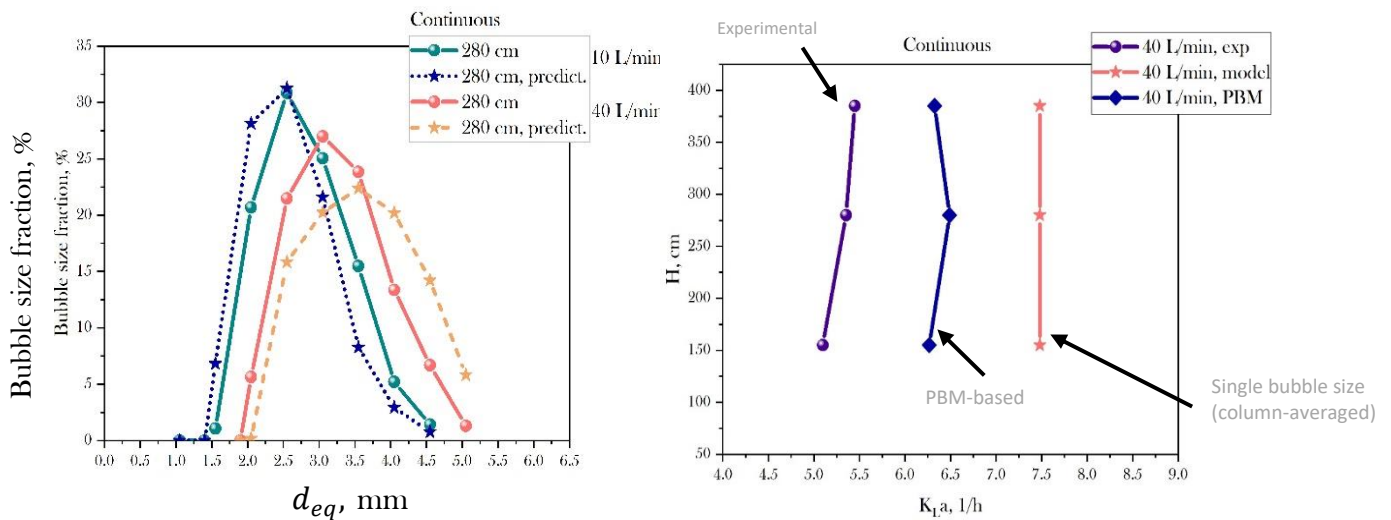
Figure 29 The PBM were able to predict bubble size distributions (left image) and the prediction of the mass transfer coefficients could be improved compared to the Higbie-based model using the average bubble size (right image).

5.2   Mass transfer modelling

Model description

For performance assessment of gas injection systems, it is crucial to know the upper limits of gas, which can be dissolved per volume per hour. A model was developed to calculate the maximum oxygen, which can be transferred per hour. The model is implemented to enable fast calculations based on models for gas-liquid mass transfer and free rising bubbles. Models for mass transfer, bubble rise velocity, interfacial area, gas hold-up, oxygen saturation were selected to predict the theoretical maximum oxygen mass transfer (Figure 30). Oxygen consumption by microorganisms can be included in the model in a later stage. Currently, the implementation is able to output the resulting mass transfer rates, standard oxygen transfer rates and aeration efficiencies depending on the bubble size as main input parameter.
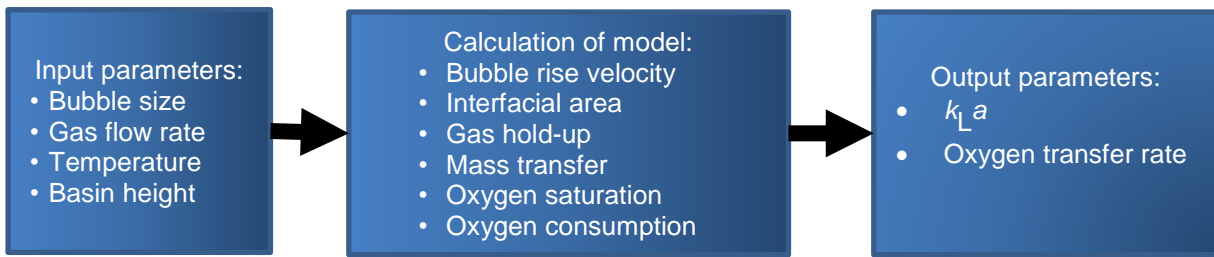
Figure 30 Parameters and included models for the calculation of the oxygen mass transferable per volume and time.

6 Hardware & Software Development

6.1 In-Situ flow microscope

Bubble Size Measurement with Flow Microscope

Techniques for measurement of gas bubble sizes in dense bubble plumes are highly demanded to investigate the performance of injection system in the laboratory and also to assist evaluation of the aeration process in the real scale. However, a robust and reliable technical solution is currently not available. Therefore, the HZDR's flow microscope has been qualified for in-situ measurement of bubble sizes. This measurement system was validated with a high-speed camera system. The result is shown in Figure 31. The results obtained with both optical measurement systems show good agreement with a deviation of below 15%.
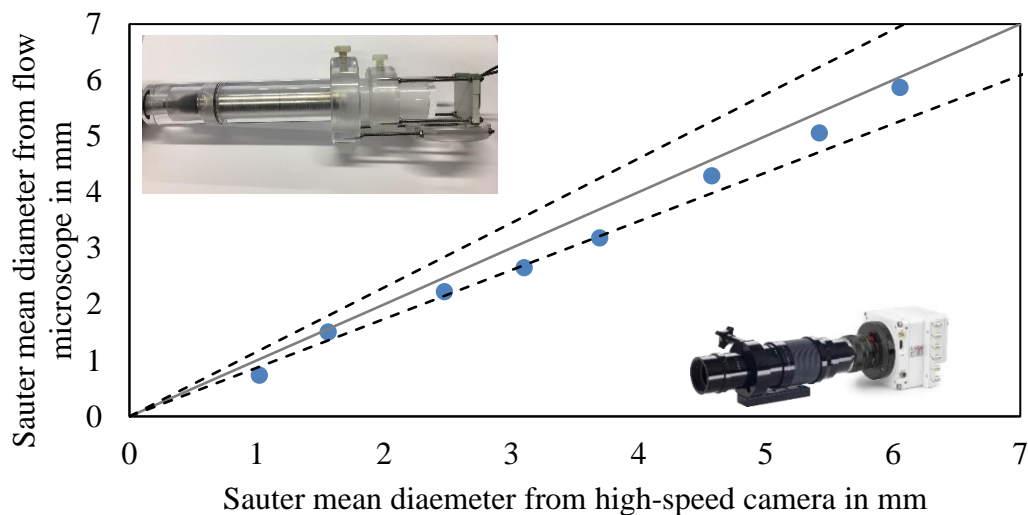
Figure 31 Comparison of Sauter mean diameter obtained from HZDR's in-situ flow microscope for bubble size measurements and high-speed camera with a deviation below 15% (dashed lines).

The microscope is equipped with a funnel for reduction of gas hold up in the optical measurement window to reduce the number of overlapping bubbles in the images. This is required in dense bubble flows and was further evaluated in an experimental investigation.

Experimental validation of funnels

The experimental setup used in this work is shown in Figure 32. The experiments were performed at different airflow conditions in a rectangular thin transparent bubble column made of acrylic glass. The two-phase flow was created by the injection of pressurized air in deionized water. For that purpose, a stainless-steel plate with a single orifice ($d_{orifice}$ = 400 μm) in the center was mounted on a special PVC block on the bottom of the column. The airflow rate through the diffusers was controlled by a mass flow controller from Omega Engineering. Two cameras, a high-speed camera and the optical flow microscope were used for image recording. The high-speed camera was installed outside of the column and its field of vision included the measurement area of the flow microscope and the bubbles entering the funnel.
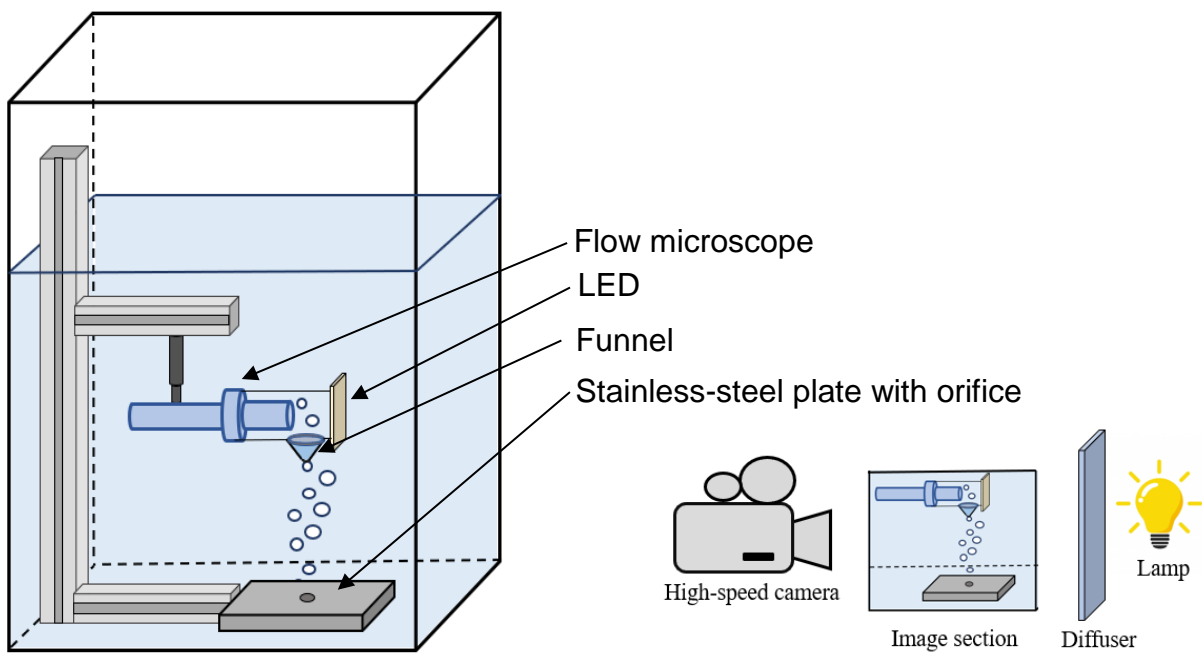
Figure 32 Sketch of the experimental setup.

The investigation included two different glass cones having 30° and 45° opening angles. The airflow rate for each installed funnel was varied in a range of 100-350 ml/min. To understand the influence of the funnel on bubble size distribution, each bubble was tracked by the flow microscope and additionally by the high-speed camera before entering the glass cone. All steps of digital image analysis like primary processing, detection and identification of the bubble's edges and determination of their spherical and Sauter mean diameters were implemented in MATLAB.

In Figure 33 the results of the image analysis in the form of variation of Sauter mean diameter versus the airflow rate are shown. The orange line represents the results achieved by high-speed camera and blue dotted line by the flow microscope. Figure 33 (a) are the results for a cone opening angle 30˚ and Figure 33 (b) for 45˚ opening angle.
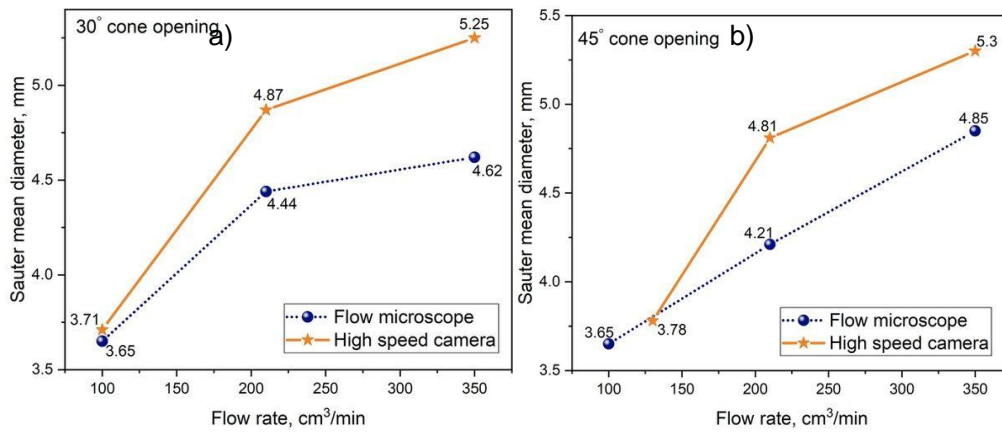
Figure 33 Sauter mean bubble diameter depending on the airflow rate and funnel's opening angle

As expected, the bubble diameter grows primary with increasing of airflow rate and it is greater for the high-speed camera measurements than for the flow microscope. Larger Sauter diameters detected by high speed camera can be explained by bubble splitting at the inlet of the funnel. The examples of such cases are given in Figure 34. If the bubble diameter exceeds the inlet diameter of the glass cones, they either break-up or do not rise into the inner region of the funnel and move further beyond (Figure 34).

Furthermore, the growing airflow rate causes a bigger difference between bubble diameters before and after entering funnel. The higher number of bubbles, their velocity and systematic turbulence with increasing airflow contribute to their more frequent splitting. As for now, there is no visible relationship between the opening angle of the cone and the diameter of the bubbles. Funnels with an optimized design and opening diameter have been manufactured and will be used in further investigations.
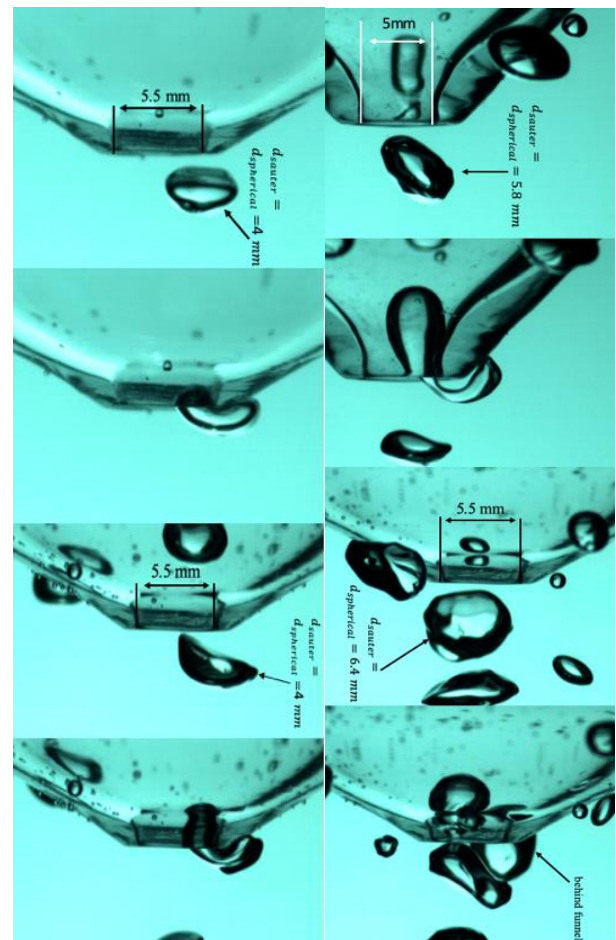
Figure 34 Bubbles splitting at the inlet of the funnel recorded by the high speed camera (left). Bubbles ($d_{saut} > d_{inlet}$) splitting recorded by high speed camera (right)

Deep tank flow microscope

Currently, bubble sizes in the literature are from
small-scale setups with simplified aerator geometries to enable bubble size measurements without overlapping bubbles. The flow microscope enables the measurement of bubble diameters in denser bubbly flows. However, the submergence was limited to about 75 cm due

29

to the short cable to the digitalization box. The available flow microscope was adapted to allow also deep tank applications under process conditions of a wastewater facility down to 5 m water column. Therefore, a cable extension was manufactured. Though, there was no image transmitted over such long distances. Therefore, the entire digitalization box was modified and fitted into an IP68 housing. A photo of the new box with the microscope is presented in Figure 35.
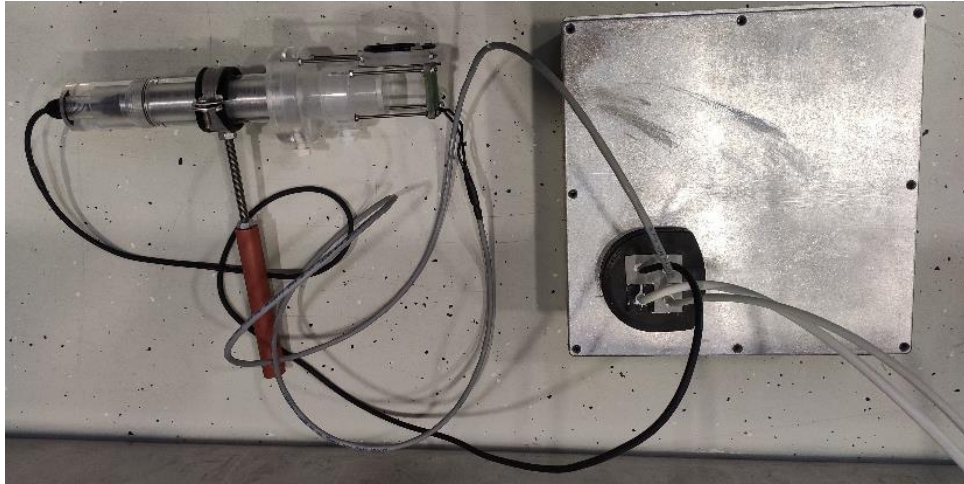
Figure 35 HZDR's flow microscope with waterproof housing for the electronics.

Only an Ethernet cable for the PC connection and a 24V power supply connection have to be provided externally. This setup has been tested in the bio-lab at HZDR with a submergence of 4.5 m and waterproofness was verified. This improved version now enables measurements in deeper basins in more realistic conditions. It will be used for bubble size measurements in pulsed aeration modes.

Figure 36 HZDR's in-situ flow microscope submerged in water experiencing bubbly flow.

6.2　Image Analysis Optimization

Images of the flow microscope were processed with bubble segmentation algorithms to detect single bubbles in the images and determine the bubble size. However, these algorithms fail if there are overlapping bubbles in the image data as shown in the following example:
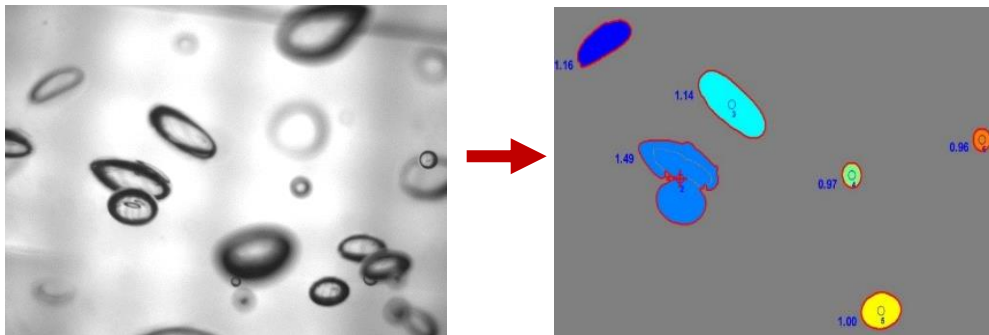
Figure 37 Bubble detection with problematic overlapping bubbles.

The overlapping bubbles could be filtered out using properties of the detected objects such as roundness. However, this method limits the possible working range for the flow microscope. The measurements could only be done for gas flow rates and gas holdups, which did not lead to too many bubbles in the field of sight.

Machine learning is used to improve the image segmentation to improve the analysis of image data. The first intermediate results showed improved bubble recognition in bubbly flows that were too dense to process it with standard algorithms:
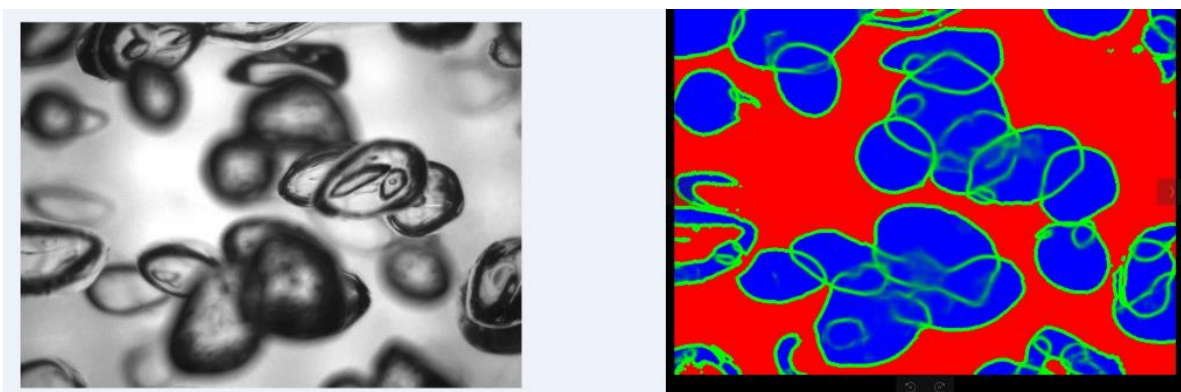
Figure 38 AI assisted bubble detection with prediction of bubble edges.

The image analysis using machine learning is still in development and is trained with larger sets of data to improve the bubble detection for difficult situations:
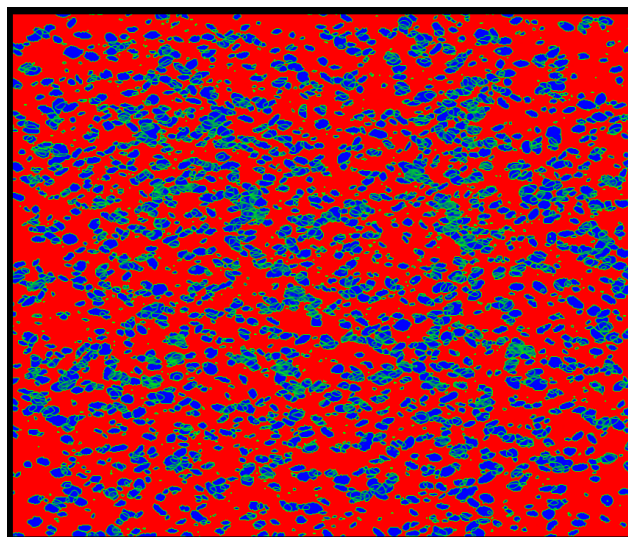
Figure 39 Example of bubble masking on a full frame image of the high speed camera.

6.3   Optimization of Pulsed Aeration Hardware

After the experimental investigations in labscale or pilot scale experiments at the wastewater treatment plant in Ottendorf-Okrilla are planned. Therefore, a gas supply system had to be designed and build. The system allows control of the gas supply to pulse the gas flow and to measure the gas flow rate accurately. It works independently from the gas supply system of the WWTP and even has a battery backup for cases of power outages.
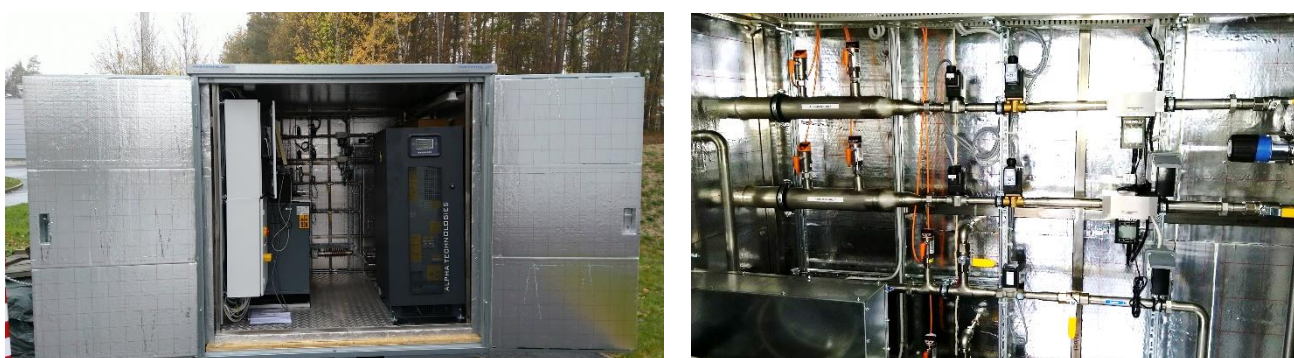
Figure 40 New gas supply system in a mobile container for the use at Ottendorf-Okrilla WWTP.

Furthermore, the mechanism to control the pulses has been improved as well. Instead of using standard solenoid valves. First tests with faster valves were conducted. Theses valves are normally used in LNG powered cars and offer faster opening times and more longevity.
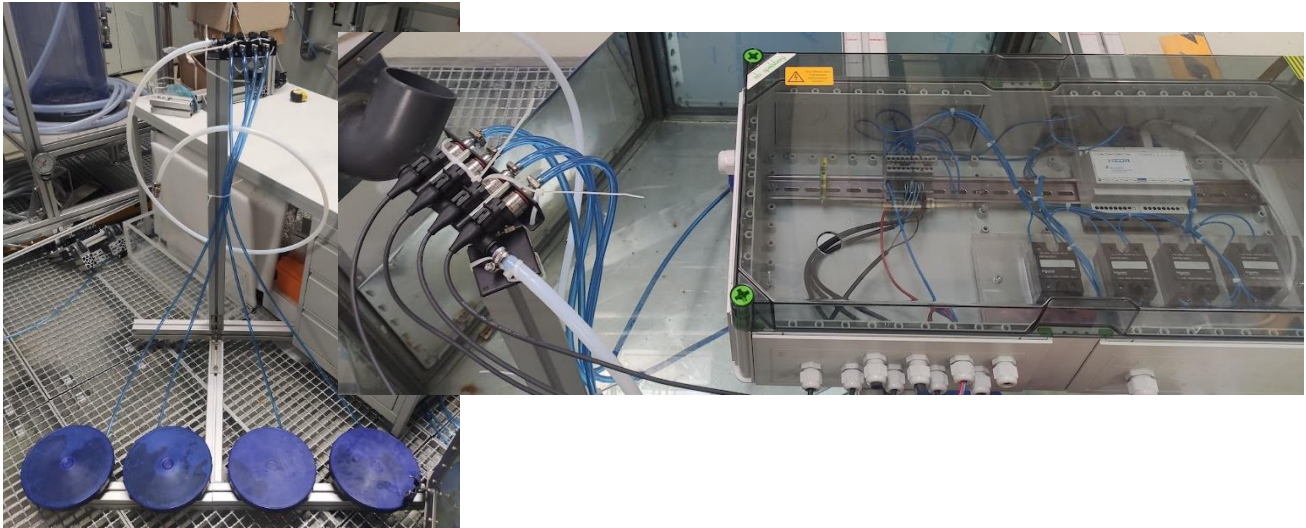
Figure 41 Gas supply for dynamic operation Implementation of fast and robust gas injection unit.

7 Additional Measurements for Air Liquide

7.1 Bubble Size Measurements with Akvola Mircobubble Generator

A first external measurement with the submergible flow microscope was conducted in AL Paris Innovation Campus in January 2021. The aim of the measurements was to evaluate the bubble size of the microbubble generator by Akvola. The tests were finished successfully and proved the capabilities of the optical measurement method. The microscopic lens enabled the measurement of bubbles even below 40 μm. Due to the small bubble diameters the bubbles were circular and there was no significant bubble overlapping. This allowed relatively fast post-processing with standard algorithms. All data regarding bubble sizes and their distribution was provided to Air Liquide.
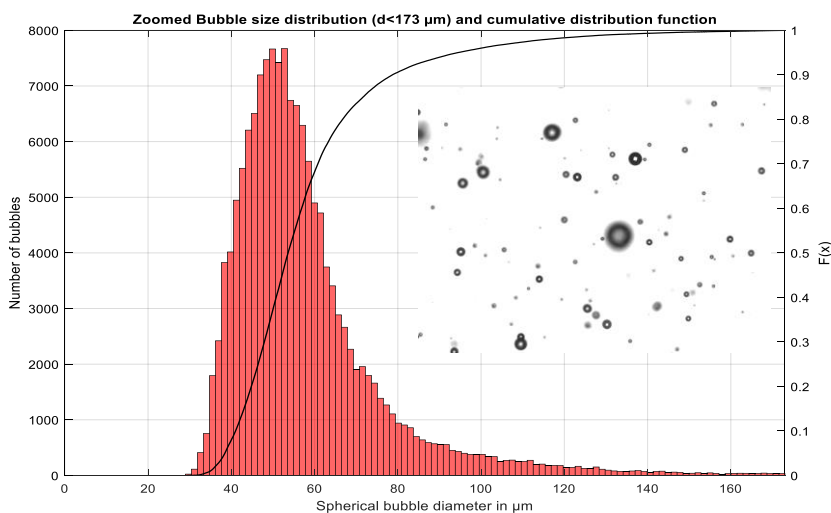
Figure 42 Example data for one experiment with the Akvola microbubble generator.

7.2 Bubble Size Measurements at Air Liquide Paris Innovation Center

The HZDR flow microscope was sent to Shanghai innovation center to enable bubble size measurements in the test setup there. Due to the global pandemic no HZDR staff could fly to Shanghai to assist in the measurements. The measurements were conducted in early 2021 and were processed in HZDR. This was the first external usage of the updated flow microscope version that allowed submergence into deeper tanks.
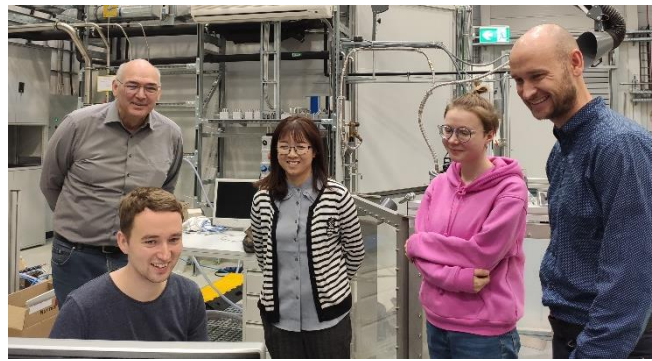
Figure 43 Participants of the first workshop at HZDR to explain the usage of the flow microscope.
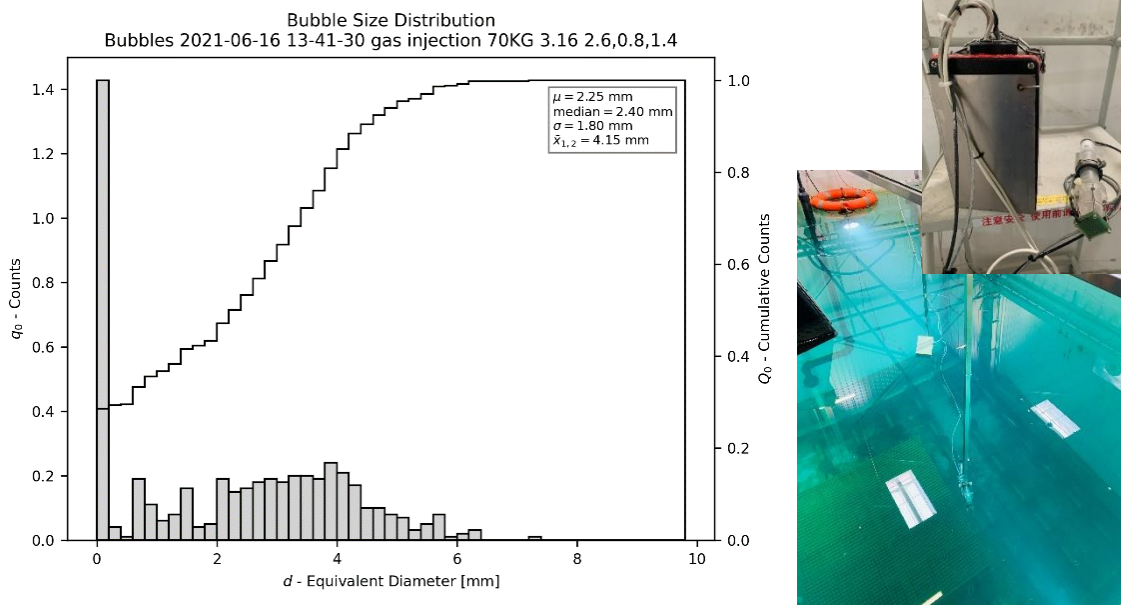
Figure 44 Sample results from experiments in Shanghai.

8   Conclusion & Outlook

The project and its investigations showed beneficial effects of pulsed aeration. It leads to higher oxygen mass transfer rates in specific cases. In narrow aeration columns positive effects could be shown for higher pulsation frequencies whereas in the DN900 column these effects were only present for higher flow rates in low frequencies. Investigations of bubble size distributions showed that the bubble size is not the only factor leading to increased oxygen mass transfer rates and that the positive effects depend on the geometry and the liquid flow behavior in the reactor. Further experiments therefore are focused on fundamental investigation the liquid flow behavior during pulsed aeration. A new experimental setup was constructed to study these hydrodynamic effects in 2D to enable a better understand of the underlying effects.

Highlights of the project:

Mass transfer during pulsed aeration
- Numerical simulations showed potential mass transfer enhancements of up to 24%
- Experimental investigations (pilot scale, DN400, 4 m aeration depth) proved mass transfer enhancements of up to 8.5% (2 Hz pulsations) confirmed in experiments in pilot scale
- DN900 column experiments showed up to 16% higher k_La in clean water (0.5 Hz) and 6.5% in wastewater (0.25 Hz)
- Optimal pulsation frequency shows a dependence of experimental geometry
- 20% improved mass transfer in wastewater pilot plant (uncontrolled aeration)
- Application of mass transfer model and population balance modelling to improve mass transfer prediction (master thesis in 2021)
- Model for scale-up and dynamic control needed and in development

Hydrodynamics during pulsed aeration
- Higher pulsation frequencies can lead to smaller bubble sizes
- Favorable range of pulse frequency of 1 to 4 s^{-1} from lab experiments
- Ideal point of operation depends on system parameters (pulse frequency, gas flow rate, vessel/tank geometry, sparger configuration)

Hardware & software development
- Waterproof flow microscope prototype for measurements down to 4.5 m water depth
- First measurement of bubble size distributions in DN900 column under pulsations
- Improvement of flow microscope accuracy
- Flexible sparger concept from MILA for spatial pulse patterns
- AI-assisted bubble recognition in images
- High potential synergies with project MILA and Advanced Process Control: align control of pulsed injection pattern with max. plant performance

9 Appendix

9.1 Index of abbreviations

CLEWATEC   Clean Water Technologies Lab

CFD   Computational Fluid Dynamics

HZDR   Helmholtz Zentrum Dresden-Rossendorf

LNG   Liquid Natural Gas

PBE   Population Balance Equation

SAE   Standard Aeration Efficiency

slpm   Standard liter per minute

SOTR   Standard Oxygen Transfer Rate

SSOTR   Specific Standard Oxygen Transfer Rate

WWTP   Wastewater Treatment Plant

9.2 Index of figures

9.3 Index of tables

9.4 References

Ammar AT Alkhalidi, Hasan B Al Ba'ba'a, and Ryoichi S Amano. Wave generation in subsurface aeration system: a new approach to enhance mixing in aeration tank in wastewater treatment. Desalination and Water Treatment, 57(56):27144-27151, 2016.

Ingmar Nopens, Elena Torfs, Joel Ducoste, Peter A Vanrolleghem, and Krist V Gernaey. Population balance models: a useful complementary modelling framework for future WWTP modelling. Water Science and Technology, 71(2):159 167, 2015.

Pöpel, H.J.; Wagner, M. Modelling of oxygen transfer in deep diffused-aeration tanks and comparison with full-scale plant data. Water Sci. Technol. 1994, 30, 71.

Doraiswami Ramkrishna and Meenesh R Singh. Population balance modeling: current status and future prospects. Annual of chemical and biomolecular engineering, 5:123-146, 2014.

CLEWATEC
Competence Center for Clean Water Technology
at HZDR

HELMHOLTZ
ZENTRUM DRESDEN
ROSSENDORF